Advanced Fiber Materials (2025) 7:315–337
https://doi.org/10.1007/s42765-024-00489-3

RESEARCH ARTICLE

Bioactive MgO/$MgCO_3$/Polycaprolactone Multi-gradient Fibers Facilitate Peripheral Nerve Regeneration by Regulating Schwann Cell Function and Activating Wingless/Integrase-1 Signaling

Zhi Yao[1] · Ziyu Chen[1] · Xuan He[4] · Yihao Wei[1] · Junyu Qian[1] · Qiang Zong[2] · Shuxian He[3] · Lili Song[6] · Lijia Ma[7] · Sien Lin[8] · Linlong Li[8,9] · Lixiang Xue[5] · Siu Ngor Fu[2] · Jin Zhang[3] · Ye Li[2,9] · Deli Wang[1]

Received: 13 May 2024 / Accepted: 29 September 2024 / Published online: 8 November 2024

Abstract
Peripheral nerve defects present complex orthopedic challenges with limited efficacy of clinical interventions. The inadequate proliferation and dysfunction of Schwann cells within the nerve scaffold impede the effectiveness of nerve repair. Our previous studies suggested the effectiveness of a magnesium-encapsulated bioactive hydrogel in repairing nerve defects. However, its rapid release of magnesium ions limited its efficacy to long-term nerve regeneration, and its molecular mechanism remains unclear. This study utilized electrospinning technology to fabricate a MgO/$MgCO_3$/polycaprolactone (PCL) multi-gradient nanofiber membrane for peripheral nerve regeneration. Our findings indicated that by carefully adjusting the concentration or proportion of rapidly degradable MgO and slowly degradable $MgCO_3$, as well as the number of electrospun layers, the multi-gradient scaffold effectively sustained the release of Mg^{2+} over a period of 6 weeks. Additionally, this study provided insight into the mechanism of Mg^{2+}-induced nerve regeneration and confirmed that Mg^{2+} effectively promoted Schwann cell proliferation, migration, and transition to a repair phenotype. By employing transcriptome sequencing technology, the study identified the Wingless/integrase-1 (Wnt) signaling pathway as a crucial mechanism influencing Schwann cell function during nerve regeneration. After implantation in 10 mm critically sized nerve defects in rats, the MgO/$MgCO_3$/PCL multi-gradient nanofiber combined with a 3D-engineered PCL nerve conduit showed enhanced axonal regeneration, remyelination, and reinnervation of muscle tissue 12 weeks post-surgery. In conclusion, this study successfully developed an innovative multi-gradient long-acting MgO/$MgCO_3$/PCL nanofiber with a tunable Mg^{2+} release property, which underscored the molecular mechanism of magnesium-encapsulated biomaterials in treating nervous system diseases and established a robust theoretical foundation for future clinical translation.

Keywords Magnesium · Multi-gradient fibers · Schwann cells · Wnt signaling pathway · Peripheral nerve regeneration

1 Introduction

Peripheral nerve defects are a prevalent and debilitating condition with limited clinical treatment efficacy [1]. The occurrence of peripheral nerve defects, predominantly in young adults, can result in lifelong disability, thereby imposing a substantial financial burden on patients [2]. Nerve defects typically require repair through nerve transplantation or bridging with various biological materials [3, 4]. Although autologous nerve transplantation remains the preferred clinical treatment option, the source of autologous nerves is limited, and their removal can lead to potential complications [5]. Therefore, designing and developing novel nerve grafts while investigating the fundamental mechanisms that promote nerve regeneration, aiming to enhance the efficacy of peripheral nerve repair, is of significant clinical importance [6, 7].

Various biomaterials containing magnesium have garnered significant attention due to their exceptional biocompatibility [8], controllable mechanical properties [9], and degradation characteristics [10]. Research has demonstrated that magnesium ions (Mg^{2+}) can effectively facilitate peripheral nerve regeneration [11, 12]. Mg^{2+} administration was beneficial in promoting Schwann cell proliferation and axonal growth in vitro by facilitating cell attachment,

Zhi Yao, Ziyu Chen and Xuan He have contributed equally to the work.

Extended author information available on the last page of the article

inducing neurite outgrowth, and enhancing nerve growth factor (NGF) secretion [13]. The implantation of Mg filaments was reported to promote axonal regeneration and remyelination in vivo [14]. Meanwhile, the deposition of inflammatory cells (such as macrophages) and the expression of inflammatory cytokines could be suppressed by either local or systemic Mg^{2+} treatment [15, 16]. Therefore, the utilization of magnesium-encapsulated nerve scaffolds in repairing peripheral nerve defects holds substantial therapeutic potential and considerable scientific research value. In previous research conducted by our group, a novel injectable magnesium-encapsulated hydrogel was developed and validated as a safe and efficacious candidate for peripheral nerve injury repair through both in vivo and in vitro experiments [17]. However, the rapid release of Mg^{2+} within the hydrogel has restricted its effectiveness solely to the early stages of nerve regeneration, as it failed to impact nerve repair during the intermediate and late stages. Furthermore, the critical signaling pathways and mechanisms by which magnesium-encapsulated nerve scaffolds regulate peripheral nerve defect repair remain unclear. Consequently, comprehensively exploring the regulatory effect of Mg^{2+} on pivotal cells and the local microenvironment during the process of nerve regeneration while establishing a rational and practical sustained Mg^{2+} release system will provide an essential theoretical foundation for the clinical translation of magnesium-encapsulated nerve scaffolds.

Schwann cells, being the most crucial functional cells in the peripheral nerve regeneration process following injury, play a dominant role throughout the entire process of nerve regeneration and repair [18]. The limited proliferative capacity and functionality of Schwann cells within the nerve scaffold are key factors contributing to the suboptimal repair of nerve defects. Following the bridging graft for repairing a 10 mm sciatic nerve defect in rats, which is the most commonly used animal model for testing biomaterial efficacy in nerve injury repair, axonal regeneration can be observed within 2 weeks. The critical period for axonal myelination and reinnervation occurs between 4 and 6 weeks post-surgery, and these processes are highly dependent on the functionality of Schwann cells [19]. Hence, the sustained-release Mg^{2+} system is anticipated to yield a consistent and prolonged impact over a 6-week period to enhance the function of Schwann cells during the middle and late stages of nerve regeneration and achieve better treatment outcomes.

Although numerous approaches can achieve the sustained release of Mg^{2+} from a materials science perspective [20], the design of magnesium-encapsulated nerve scaffolds needs to consider various requirements [21], including mechanical properties, the duration of release, and potential neurotoxicity that result from the excessive and premature release of Mg^{2+} [22]. Electrospinning is a versatile and cost-effective technique that harnesses the electrostatic repulsion between surface charges to continuously extrude nanofibers from a viscoelastic fluid [23]. This approach has been widely employed for fabricating nanofibers with diameters as small as tens of nanometers from various materials [24]. Reorganizing the alignment, stacking, and/or folding of electrospun nanofibers facilitates the formation of ordered arrays or multi-gradient structures, rendering electrospun nanofibers suitable for various applications [25–27]. Numerous research studies have opted to utilize Mg-containing monomers, such as MgO and $MgCO_3$, as alternative sources for achieving a controlled and consistent release of Mg^{2+}. The distinctive degradation properties of these materials present both challenges and opportunities. While MgO degrades rapidly, posing a challenge for long-term release, but also demonstrates antibacterial properties, $MgCO_3$ dissolves at a slower rate than MgO but contains relatively lower levels of effective Mg^{2+}. Adjusting the concentration and ratio of the Mg monomer makes it feasible to achieve the sustained release of Mg ions. Although this sustained-release system has demonstrated efficacy in bone defect models, its potential application in nerve defects remains unexplored [28].

In this study, electrospinning technology was employed to fabricate a multi-gradient nanofiber membrane consisting of MgO/$MgCO_3$/polycaprolactone (PCL), with the objective of enhancing peripheral nerve regeneration. Adjusting the concentration and proportion of the Mg monomer and the number of electrospun layers, integrating both rapidly degradable MgO and slowly degradable $MgCO_3$ into scaffolds, has proven to be an effective approach for precisely regulating the release of Mg^{2+} for peripheral nerve regeneration. A comprehensive evaluation of the nanofibrous structure, surface properties, and biomolecular composition of the membrane was performed. The integration of MgO/$MgCO_3$/PCL multi-gradient fibers with a 3D-engineered PCL conduit was employed for the in vivo repair of peripheral nerve defects. The safety and efficacy of the material for in vivo implantation were comprehensively assessed, and its effectiveness for axonal regeneration, myelination, and reinnervation was validated. Finally, a comprehensive investigation was conducted to elucidate the underlying mechanisms of Mg-induced nerve regeneration in vitro, leading to a thorough understanding of the pivotal signaling pathways and regulatory mechanisms of magnesium ions in modulating Schwann cell function. Building upon previous research, this study modified the sustained Mg^{2+} release system and expanded the theoretical foundation of Mg^{2+} in peripheral injury treatment, thus providing an essential theoretical basis and empirical evidence for the advancement and application of magnesium-encapsulated neural scaffold materials.

2 Experimental Section

2.1 Study Design

In this project, PCL was mixed with different concentrations of magnesium monomers (MgO and $MgCO_3$) and processed into a multi-gradient nanofiber membrane using electrospinning technology. The material was further characterized using scanning electron microscopy to analyze the fiber size, degradation, and release of magnesium ions. A primary culture of dorsal root ganglia (DRG) and Schwann cells was utilized to screen for the optimal concentration of Mg^{2+} to further elucidate the mechanism by which Mg^{2+} promotes peripheral regeneration. Axonal length and Schwann cell proliferation and migration were measured to determine the effect of Mg^{2+} on axonal growth and Schwann cell behavior. In vitro RSC96 cell line cultures were used to verify the proliferation and migration of Schwann cells induced by various concentrations of Mg^{2+} using the CCK-8 test and cell scratch test, respectively. Ribonucleic acid (RNA) sequencing was employed to detect gene expression regulation and key signaling pathways during Mg^{2+}-induced nerve regeneration. Lastly, gene expression in RSC96 cell cultures was analyzed using western blots. A 10 mm sciatic nerve defect model was established in 45 Sprague–Dawley (SD) rats divided into five groups based on the different repair materials used. In the experimental group, multi-gradient fibers with varying concentrations of Mg^{2+} were implanted into a 3D-engineered PCL nerve conduit (autograft, PCL, 10% MgO/$MgCO_3$/PCL, 20% MgO/$MgCO_3$/PCL, and 30% MgO/$MgCO_3$/PCL). Nerve and muscle samples were collected 6 weeks and 12 weeks post-surgery. Histological staining, transmission electron microscopy analysis, and gait analysis were carried out to evaluate nerve regeneration and motor function recovery.

2.2 Preparation of MgO/$MgCO_3$/PCL Multi-gradient Nanofiber Membrane

The PCL was blended with varying concentrations of magnesium-containing monomers (MgO and $MgCO_3$) to produce a highly refined polymer powder. The plastic powder was then heated until it was transformed into a molten viscous substance, which was subsequently electrospun utilizing a high-voltage electric field (TL-01, Tongli Technologies Co., China). Three sets of MgO/$MgCO_3$/PCL membranes were prepared in our study, with a total weight/weight ratio of Mg monomers to PCL at 10%, 20%, and 30%, respectively. The MgO/$MgCO_3$/PCL membrane was fabricated in a trilamellar configuration, where the weight ratio of total MgO/$MgCO_3$ decreased progressively from inner layer to outer layer. The inner and outer layer exhibited a respective 20% increase and decrease in the concentration of Mg monomers when compared to the intermediate layer. Additionally, the compositions of Mg monomers exhibited layer-dependent variations, with an uptrend of $MgCO_3$ observed in the inner layer, and a corresponding uptrend of MgO in the outer layer. Notably, the ratios of MgO to $MgCO_3$ transitioned from 1:2 at the inner layer, through 1:1 in the intermediate layer, to 2:1 at the outer layer. The convergence of these two parameters—the concentration of Mg monomers and the compositional makeup of Mg monomers—ultimately culminated in the development of a multigradient structure. The degradation properties of MgO/$MgCO_3$/PCL were evaluated through in vitro degradation tests incubated at 37 °C. The concentration of Mg^{2+} in the solution was determined using an inductively coupled plasma optical emission spectrometer (ICP-9820, Shimadzu, Japan), 1 cm × 1 cm MgO/$MgCO_3$/PCL membranes were immersed in 1 mL of PBS solution, and a sustained-release curve for Mg^{2+} was plotted. MgO/$MgCO_3$/PCL membranes (2 cm × 2 cm) were immersed in 4 mL of PBS at 37 °C and meticulously weighed. Subsequently, the membranes were rinsed with Milli-QH_2O, dried at 37 °C, and re-weighed at specific time points (day 3; week 1–4) to determine the percentage of weight loss.

2.3 Morphology and Hydrophilicity Analysis of MgO/$MgCO_3$/PCL Multi-gradient Nanofiber Membranes

The MgO/$MgCO_3$/PCL multi-gradient nanofiber membranes were treated with 2.5% glutaraldehyde for 6 h, followed by three rinses in deionized water (each for 30 min) and dehydration in a graded alcohol series (30%, 50%, 75%, and 100% ethanol) for 30 min each. Subsequently, the membranes were dried using a critical point dryer after being balanced with 100% ethanol. A thin layer of platinum and gold mixture was applied to enhance conductivity and contrast prior to observing the micromorphology observed by scanning electron microscopy (SEM; S-8010, HITACHI, Japan) at an accelerating voltage of 5 keV. Image analysis software (ImageJ; Cybernetics, Bethesda, MD, USA) was utilized to assess the structural fiber parameters [29]. The morphologies of the MgO/$MgCO_3$/PCL membranes were also examined via SEM at the 4-week timepoint to analyze in vitro degradation. Eventually, the energy dispersive X-ray spectroscopy (EDS) analysis and mapping were utilized to validate the variation in Mg elemental proportion from the inner to the outer layers within each set of MgO/$MgCO_3$/PCL membrane.

The surface wettability of the MgO/$MgCO_3$/PCL multi-gradient nanofiber membranes was further characterized by

determining the contact angles of five groups of materials using the Modified Wilhelmy Plate method [30]. During the measurements, the sample surface to be analyzed was suspended on a force sensor instead of a metal sheet and gradually immersed into the liquid phase. The change in force was recorded to calculate the advancing contact angle value between the liquid and solid surfaces. Subsequently, the solid sample was slowly withdrawn from the liquid phase while changes in force were recorded to determine the receding contact angle value.

2.4 Preparation of 3D-Engineered PCL Conduit

A nerve conduit is necessary for repairing nerve continuity in an animal model with nerve defects. Therefore, the 3D-engineered PCL nerve conduit from our previously published article was utilized for this study [17]. The PCL conduits were created using a 3D printing technique (Shanghai Graphic Design Information Co., China) [17]. Specifically, a 200 μm diameter PCL filament was printed on a rotating stainless-steel disk with a diameter of 2 mm for 30 min. Subsequently, the conduits were removed from the disk and vacuum-dried for 24 h.

2.5 DRG Neuron Neurite Extension Assay

DRGs were collected from 2- to 4-week-old SD rats to elucidate the role of Mg^{2+} in facilitating the axonal outgrowth of DRG neurons. Bilateral DRGs were cultured in vitro in a 35 mm culture dish and studied under a microscope. Next, we removed neuronal fibers connected to the DRGs. DRGs were plated in Matrigel-precoated (356234, Corning) 35 mm dishes, cultured with Neurobasal medium (A358290, Thermo Fisher Scientific) containing 2% B-27 supplement (A3582801, Thermo Fisher Scientific), 0.3% L-glutamine (25030081, Thermo Fisher Scientific), 100 ng/mL NGF (N2513, Sigma-Aldrich), and 1% Penicillin–Streptomycin–Neomycin (PSN) antibiotic mixture in a 37 °C incubator with 5% CO_2 and 92% humidity [31]. The medium was changed every day [31]. Additional Mg^{2+} was directly added to the medium (four groups: Ctrl, 10 mM Mg^{2+}, 20 mM Mg^{2+}, and 30 mM Mg^{2+}). DRG neurites with extended neurites were imaged and quantified manually after 5 days of incubation. The longest neurite extension distance was calculated every 15° in each direction.

2.6 Primary Schwann Cell Culture

Bilateral sciatic nerves were collected from 2- to 4-week-old SD rats to investigate the effects of Mg^{2+} on the proliferation, migration, and phenotypic conversion of Schwann cells. Schwann cells were isolated from the nerves by sequential digestion in papain and type I collagenase (1.0 mg/mL) for 3 h. The isolated cells (5000 cells/mL) were cultured in Dulbecco's modified Eagle medium (DMEM)/10% fetal bovine serum (FBS; 11320033, Thermo Fisher Scientific) overnight. The medium was replaced with DMEM/10% FBS supplemented with 10 μM cytosine arabinoside (Ara-C; 449651000, Thermo Fisher Scientific), and Schwann cells were cultured for an additional 48 h to remove mitotic cells. Afterward, the medium was replaced with DMEM/10% FBS supplemented with 2 μM forskolin and additional Mg^{2+} (four groups: Ctrl, 5 mM Mg^{2+}, 10 mM Mg^{2+}, and 15 mM Mg^{2+}). Morphological changes in the Schwann cells were observed as the culture time increased, and the cell count in different groups was recorded [32].

2.7 Quantitative Real-Time PCR

Primary Schwann cells were harvested on day 5, and total RNA was isolated using TRIzol reagent (15596026; Invitrogen, Waltham, MA, USA). The concentration and purity of the RNA were assessed with a NanoDrop 2000 (Thermo Fisher Scientific, USA), followed by reverse transcription to cDNA using the First Strand cDNA kit (Takara, Dalian, China). Real-time quantitative PCR (RT-qPCR) analysis of the cDNA template was conducted using TF pack power SYBR Green qPCR SuperMix-UDG. The levels of gene expression for axon guidance molecules (including netrins, slits, ephrins, and semaphorins) [17], neurotrophic factors (NGF, brain-derived neurotrophic factor (BDNF), and vascular endothelial growth factor (VEGF)), the Wingless/integrase-1 (Wnt) family (Wnt 1, Wnt2, Wnt3a, Wnt5a, Wnt5b) [33], and C-Jun [34] were evaluated. The primer sequences used in this study are shown in Table S1 (Supporting Information). A gene expression heatmap was created using www.heatmapper.ca/expression/, with the target gene expression levels normalized to that of GAPDH.

2.8 In Vitro RSC96 Cell Culture

RSC96 cell culture was carried out to verify the biocompatibility of the MgO/$MgCO_3$/PCL membrane, and the regulatory effect along with its mechanism of Mg^{2+} on Schwann cells. A frozen 1 mL cell suspension was thawed by vigorously shaking the tube in a water bath at 37 °C; then, it was mixed with 4–6 mL of complete medium in a centrifuge tube. The supernatant was decanted after centrifugation, and the cells were resuspended in a fresh, complete medium. The cell suspension was transferred to a culture dish containing 6–8 mL of a complete medium and incubated overnight at 37 °C. Microscopic examination was performed the following day to assess cell growth and density before continuing with the culture process. The cells were cultured in DMEM/10% FBS in an incubator maintained at 37 °C

with a CO_2 concentration of 5%, and media changes were performed every other day[35].

2.9 CCK-8 Assay of Cell Viability and Cell Proliferation

The CCK-8 assay was conducted to identify the most effective concentrations of Mg^{2+} for enhancing cell viability and cell proliferation in Schwann cells. RSC96 cells were suspended in optimal growth conditions, and 100 µL of the suspension was added to each well of a 96-well cell culture plate at a density of 2×10^3 cells/100 µL. Various concentrations of Mg^{2+} (Ctrl, 1, 2, 5, 10, 15, 20, 25, 30, and 35 mM) were added to the culture wells and incubated at 37 °C for either 24 or 48 h. Following this incubation, 10 µL of CCK-8 solution from the kit was added to each well before measuring the absorbance at a single wavelength of 450 nm for detection purposes [9].

2.10 Cell Scratch Assay

The cell scratch assay was performed to assess the impact of Mg^{2+} on cellular migration. RSC96 cells were seeded in a six-well plate with 2.0 mL of medium per well and reached confluence within approximately 24 h. A line was marked at the bottom of each well to ensure proper alignment, and caution was taken to maintain the vertical orientation of the pipette while aspirating the culture supernatant and rinsing away any detached cells with PBS. Four experimental groups were tested: Ctrl, 5 mM, 10 mM, and 15 mM Mg^{2+} [36]. Subsequently, 2 mL of serum-free medium was added to each well before incubating the plates further. Samples were collected at 0, 48, and 96 h time points to monitor changes in cell migration by photography.

2.11 Transcriptome Sequencing of Mg^{2+}-Induced Peripheral Nerve Regeneration

This study utilized transcriptome sequencing to systematically investigate the impact of Mg^{2+} on gene expression during nerve regeneration. Total RNA was extracted from two sets of RSC96 cell culture samples (Ctrl and 10 mM Mg^{2+}-treated). RNA purity was assessed using the NanoDrop™ One/OneC by measuring OD260/280 and OD260/230 ratios. Accurate quantification of RNA was conducted using the Qubit™ RNA HS Assay Kit on the Life Invitrogen Qubit® 3.0 fluorescence quantitative instrument. The Agilent 4200 TapeStation system was used to precisely evaluate RNA integrity.

After determining the quality of the samples, a sample library was constructed. Since most eukaryotic mRNA contains a polyA structure, magnetic beads with oligo (DT) were employed to capture mRNA with this structure. The first cDNA strand was then synthesized using fragmented mRNA as a template and random oligonucleotides as primers in the M-MuLV reverse transcriptase system. Ribonuclease H (RNaseH) was used to degrade RNA strands, followed by the synthesis of second-strand cDNA from dNTPs using the DNA polymerase I system. The double-stranded cDNA was subsequently purified and subjected to end repair, A-tail addition, and sequencing adaptor ligation. Subsequently, approximately 200 bp cDNA fragments were selected using AMPure XP beads, followed by PCR amplification and further purification of the PCR products using AMPure XP beads to obtain the sequencing library. Reproducible library concentration quantification was achieved using Kapa qPCR, and the Agilent 4200 TapeStation assay was used to accurately determine library fragment size. Following the confirmation of library quality, they were pooled based on the required concentration and the desired data quantity before undergoing Illumina PE150 sequencing.

2.12 Bioinformatics Analysis

The specific process for bioinformatics analysis involves: (1) performing data quality control; (2) aligning the clean data to the reference genome and conducting statistical analysis; (3) quantifying gene expression based on the alignment results with a focus on sequencing coverage (read count) for each gene; (4) analyzing the differentially expressed genes between samples or groups to identify significant differences in gene expression; (5) performing functional enrichment analysis and obtaining protein interaction data based on the differential expression of genes between samples or groups by leveraging functional annotation databases such as Gene Ontology (GO), Kyoto Encyclopedia of Genes and Genomes (KEGG), and STRING; (6) detecting variants by analyzing single nucleotide polymorphisms (SNPs), indels, alternative splicing events, fusion genes and annotations using transcriptome data, which enables the exploration of disease or phenotype-related information at the transcriptome level; and (7) gene set enrichment analysis (GSEA) and immune infiltration analysis using the quantitative gene expression results[37].

2.13 Western Blotting

The effect of Mg^{2+} on the regulation of the Wnt signaling pathway was investigated in RSC96 cells cultured for 24 h in 4 different groups (Ctrl, 5, 10, and 15 mM Mg^{2+}). The medium was then replaced with the treatment reagents. In vitro, siRNA transfection (siRNA ID#: 121949, Thermo Fisher Scientific) was used to knockdown Wnt5a expression in four groups (Ctrl, 10 mM Mg^{2+}, Mg^{2+} with Lipo:Wnt5a-siRNA, and Mg^{2+} with Lipo:blank). Finally, nifedipine and calcium chloride were added to the medium in four other

treatment groups (Ctrl, 10 mM Mg^{2+}, 10 mM Mg^{2+} with 10 mM Ca^{2+}, and 10 mM Mg^{2+} with nifedipine). The cells were cultured for 24 h, followed by treatment with a radioimmunoprecipitation assay buffer containing a proteinase/phosphatase inhibitor mixture to extract the proteins. The isolated intact RSC96 cell proteins underwent western blot analysis using a previously established protocol [25]. Subsequently, these proteins were separated on a sodium dodecyl sulfate–polyacrylamide gel and further processed according to a previous protocol [38]. Antibodies against the following proteins were employed: Wnt5a (1:500, SAB5300184, Sigma-Aldrich), protein kinase C (PKC, 1:500, ab32376, Abcam), β-Catenin (1:500, GB15015-100, Thermo Fisher Scientific), CREB (1:500, A13819, Abclonal), C-MYC (1:500, ab32072, Abcam), and C-Jun (1:500, GB111604-100, Thermo Fisher Scientific). The expression levels of the target proteins were analyzed and normalized to those of vinculin (1:500, 700,062, Thermo Fisher Scientific).

2.14 Animals and Surgical Procedures

Forty-five female SD rats (2 months old, weighing 200–250 g) were obtained from Topbio-technology (Shenzhen, China) and housed under standard laboratory conditions with a 12 h light/dark cycle, ambient temperature of 25 °C, and humidity of 50%. The rats were provided ad libitum access to food and water. All animal experiments adhered to the Guidelines for the Care and Use of Laboratory Animals and were approved by the Animal Care and Use Committee (IACUC) of Peking University Shenzhen Hospital (No. 2023-616). The rats were randomly allocated to one of five groups: autograft, PCL nerve conduit, 10% MgO/$MgCO_3$/PCL, 20% MgO/$MgCO_3$/PCL, and 30% MgO/$MgCO_3$/PCL. For the experiential groups, the MgO/$MgCO_3$/PCL membranes were cut into multi-gradient fibers measuring 0.5 mm × 12 mm (total four fibers for each group).

The rats were anesthetized with a combination of pentobarbital sodium at a dosage of 50 mg per kg of body weight and isoflurane and then underwent microsurgery performed by the same experienced surgeon [39]. Initially, the surgical site (the lateral side of the right thigh) was prepared with draping and sterilization, followed by creating a roughly 4 cm incision parallel to the lower edge of the femur. The sciatic nerve was carefully exposed through this incision using a surgical microscope. In the autograft group, a 10 mm segment of the sciatic nerve was excised, everted, and reinserted. The autografts were secured to the epineurium of the proximal and distal nerve stumps using 10–0 monofilament nylon sutures. For the PCL nerve conduit, 10% MgO/$MgCO_3$/PCL, 20% MgO/$MgCO_3$/PCL, and 30% MgO/$MgCO_3$/PCL groups, the distal end of the exposed sciatic nerve was initially transected before advancing the nerve stumps 1 mm toward the proximal end of a 12 mm conduit (resulting in a gap of 10 mm). They were then anchored in place with 10–0 nylon sutures. With one end of the nerve conduit attached to the nerve stump, the multi-gradient fibers containing 10%, 20%, and 30% MgO/$MgCO_3$/PCL were inserted into the nerve conduit (four fibers in each conduit, each fiber with a size of 0.5 mm × 12 mm), and the other end of the nerve conduit was attached to the distal nerve stump. The conduit diameter (approximately 2 mm) matched that of the sciatic nerve. Finally, the skin wound was closed using 4–0 silk sutures.

2.15 Histological Evaluation and Transmission Electron Microscopy Analysis of Regenerated Nerves

Regenerated nerves were harvested at the 6- and 12-week follow-up examinations by perfusing a 4% paraformaldehyde solution through the circulatory system of the rats [40]. The nerve graft was divided into three equal parts: proximal, middle, and distal. Cross-sections of the middle region were sliced to a thickness of 7 μm using a Leica CM3050S microtome. These sections were then subjected to hematoxylin and eosin (H&E) staining. Subsequently, the images from five random fields for each section were analyzed, and statistical analysis was performed on 4 samples from each group. Immunohistochemical analysis of C-Jun (1:200; SRP2088; Sigma-Aldrich) expression was performed in nerve samples at 6 weeks post-surgery.

The distal areas of the nerve grafts were examined by toluidine blue staining and transmission electron microscopy (TEM). A 2 mm portion of the regenerated nerve was treated with 2.5% glutaraldehyde for 2 h, followed by post-fixation in 1% osmium tetroxide for 1.5 h. The tissue samples were dehydrated in an ethanol series, embedded in Epon 812 resin (Ted Pella, Redding, CA, USA), and then cut into semi-thin sections of 1 μm and ultrathin sections of 50 nm. The semi-thin sections were stained with a toluidine blue solution, and the ultrathin sections were examined using TEM (JEOL, Tokyo, Japan). Five random fields in each section were chosen for image capture. The myelinated axon diameter and myelin sheath thickness were measured using Photoshop CS6 software (Adobe Systems). The G ratio was calculated as the ratio of axon diameter to fiber diameter. Analysis was conducted on photographs from five random fields in each ultrathin nerve section, with statistical analysis performed on five samples from each group.

2.16 Morphometric Examination of Reinnervated Muscles

The bilateral triceps surae muscles were collected from each group 12 weeks post-surgery. The muscles were fixed, embedded in paraffin, and transversely sectioned

for Masson's trichrome staining (ab150686, Abcam). Four samples from each time point in each group were stained, and five randomly selected fields in each specimen were photographed [17]. Subsequently, ImageJ software (Media Cybernetics, Bethesda, MD, USA) was used to measure the cross-sectional areas of the muscle fibers. The percentage of collagen fibers was determined by dividing the area occupied by collagen fibers by the total area encompassing both collagen and muscle fibers.

2.17 Functional Evaluation of Nerve Regeneration

The recovery of regenerated nerves was evaluated first using the sciatic functional index (SFI). Briefly, rats were trained to walk on a glass surface to reach food pellets at one end of a track. Their movements were recorded from below as they crossed the track in a dark room, allowing for clear differentiation between paw prints. Data on paw length (PL), toe spread (TS), and intermediary toe spread (IT) were collected for both normal (N) and experimental (E) hind legs. The SFI was then calculated using a previously established formula (1) [41]:

$$\begin{aligned} \mathrm{SFI} = & -38.3 \times \left(\frac{\mathrm{EPL}-\mathrm{NPL}}{\mathrm{NPL}}\right)+109.5 \\ & \times \left(\frac{\mathrm{ETS}-\mathrm{NTS}}{\mathrm{NTS}}\right)+13.3 \times \left(\frac{\mathrm{EIT}-\mathrm{NIT}}{\mathrm{NIT}}\right)-8 \end{aligned} \quad (1)$$

Electrophysiological assessment was performed on rats in all five experimental groups to evaluate the functional recovery of nerve regeneration 12 weeks after nerve graft implantation. Four rats from each group were anesthetized, electrical stimuli were applied to the nerve trunk at the proximal end of the graft site and CMAPs were recorded by placing the signal-receiving electrode at the triceps surae muscles by a portable biological-function experimental system (BL-420F; TaiMeng, Chengdu, China). The stimulating mode was set as the pulse mode (stimulus intensity = 10 mV; frequency = 1 Hz; duration = 1 ms).

2.18 Statistical Analyses

The data were reported as the mean ± standard deviation. Statistical variances were analyzed using a one-way factorial analysis of variance and Tukey's post hoc test. GraphPad Prism 6.01 (GraphPad Software, Inc.) was employed for statistical analyses, with significance set at $P < 0.05$.

3 Results and Discussion

3.1 Fabrication and Characterization of MgO/$MgCO_3$/PCL Multi-gradient Nanofiber Membranes

Mg^{2+} plays a crucial role in various pathophysiological processes, including energy metabolism, nerve impulse generation and transmission, and muscle contraction [42]. From a neuroscientific perspective, Mg^{2+} is indispensable for neuromuscular coordination [43], nerve impulse propagation, and neuroprotection [44]. Its potential involvement in the peripheral nervous system includes exerting neuroprotective effects, suppressing inflammation, and promoting nerve regeneration. In recent years, significant emphasis has been placed on various magnesium-encapsulated biomaterials used as therapeutic carriers for delivering Mg^{2+} [45]. Compared to traditional implant materials, these biomaterials offer numerous advantages [46], such as exceptional biocompatibility, controllable specific strength and stiffness properties, degradability characteristics, and abundant resources at a low cost [47]. Numerous studies have used MgO as an alternative source for achieving a controllable and consistent release of Mg^{2+} due to its rapid degradation [48], which poses challenges for long-term release but also exhibits antibacterial properties. In contrast, while $MgCO_3$ dissolves at a slower rate than MgO, it contains relatively lower levels of effective Mg^{2+} [28]. Therefore, it is reasonable to propose that integrating both rapidly degradable MgO and slowly degradable $MgCO_3$ into scaffolds would be an effective approach for precisely regulating the release of Mg^{2+} for peripheral nerve regeneration.

In this study, multi-layered nanofiber membranes were produced using a combination of PCL and varying concentrations of magnesium monomers (MgO and $MgCO_3$). A series of membranes composed of MgO/$MgCO_3$/PCL was created using the electrospinning technique, consisting of three sets with varying ratios of Mg monomers to PCL, at 10%, 20%, and 30%. Each membrane was composed of three layers, with a decreasing proportion of MgO/$MgCO_3$ from layer to layer and a gradual reduction in the concentration of Mg monomers from inner to outer. Notably, the Mg monomer proportions differed across the three layers, with the inner layer containing more $MgCO_3$ and the outer layer containing more MgO, resulting in the development of a multi-gradient structure (Fig. 1A). The degradation characteristics of MgO/$MgCO_3$/PCL were assessed through in vitro experimentation, which showed a sustained Mg^{2+} release profile (Fig. 1B). Among the three groups, the 10% MgO/$MgCO_3$/PCL membrane exhibited the most effective and stable release of Mg^{2+}, which was sustained within 1–6 weeks and reached a plateau after 7 weeks. The release rate of the

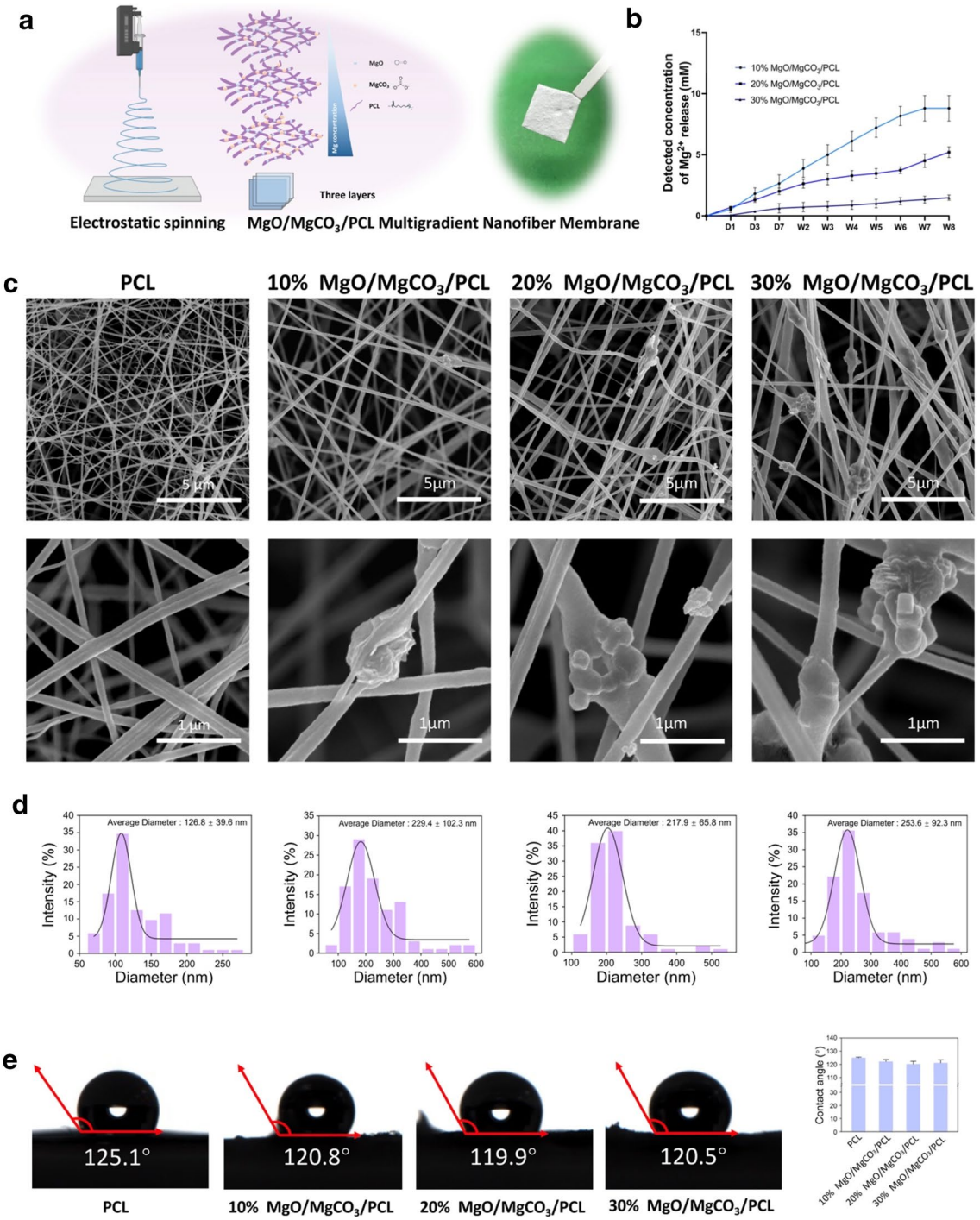

Fig. 1 MgO/$MgCO_3$/PCL multi-gradient nanofiber membrane fabrication and characterization. **a** Fabrication of MgO/$MgCO_3$/PCL multi-gradient nanofiber membranes. **b** Cumulative Mg^{2+} release from MgO/$MgCO_3$/PCL multi-gradient nanofiber membranes over 6 weeks. **c** SEM characterization of MgO/$MgCO_3$/PCL multi-gradient nanofiber membranes. **d** Calculation of the diameter of the nanofibers. **e** Measurement of the contact angles of the MgO/$MgCO_3$/PCL multi-gradient nanofiber membranes

20% and 30% MgO/$MgCO_3$/PCL membranes within 8 weeks was slower than that of the 10% group, with the peak Mg^{2+} release not reached within the detection time of this study.

Our findings suggested that the MgO/$MgCO_3$/PCL system could achieve the tunable and sustained release of Mg^{2+}. In contrast to the rapid degradation within 2 weeks observed in our previously published study involving a Mg^{2+}-containing

hydrogel [17], this multi-gradient nanofiber membrane composed of MgO/$MgCO_3$/PCL demonstrated the effective and sustained release of Mg^{2+} for 4–6 weeks, depending on the magnesium concentration. By incorporating both rapidly degradable MgO and slowly degradable $MgCO_3$ into the MgO/$MgCO_3$/PCL system, the release of Mg^{2+} could be effectively regulated. Consequently, the sustained release performance of the modified material was predominantly influenced by two pivotal factors: the overall concentration of Mg monomer and the proportion of $MgCO_3$. A higher concentration of mixed Mg monomer or a greater proportion of $MgCO_3$ decelerated the release of Mg^{2+}. One limitation of this study was the relatively short detection time for the Mg^{2+} release properties. The release from the 20%/30% MgO/$MgCO_3$/PCL membranes during the initial 8 weeks was observed to be weaker than that of the 10% group. The reason for the slower release of Mg^{2+} from fiber membranes with higher concentrations of Mg monomers potentially attributed to various reasons. The increased total amount of $MgCO_3$ might lead to a delayed release of Mg^{2+}. Furthermore, the higher concentration of total Mg monomers resulted in an enhanced crosslinking degree between PCL and Mg, thereby tightening the material. This could potentially cause a slight alteration in material thickness, ultimately leading to a non-linear relationship between the concentration of Mg monomer and sustained release rate of the material. Based on our current research findings, we are unable to definitively confirm the aforementioned idea. However, this finding also highlighted the potential of the tunable Mg^{2+} release system to customize formulations based on varying sustained-release requirements.

3.2 SEM and Surface Property Analysis of MgO/$MgCO_3$/PCL Multi-gradient Nanofiber Membranes

The SEM analysis provided detailed insight into the multi-gradient nanofiber reticular structure, revealing an interconnected network of nanofibers with MgO/$MgCO_3$ nanoparticles distributed throughout (Fig. 1C). The average diameter of the nanofibers was 126.8 ± 39.6 nm in the control group (PCL), 229.4 ± 102.3 nm in the 10% MgO/$MgCO_3$/PCL group, 217.9 ± 65.8 nm in the 20% MgO/$MgCO_3$/PCL group, and 253.6 ± 92.3 nm in the 30% MgO/$MgCO_3$/PCL group (Fig. 1D). SEM scanning was also applied to obtain the vertical structural characteristics of the MgO/MgCO3/PCL membrane, which revealed a cohesive integration of the tripartite layers, attributed to the tight crosslinking between each layer (Fig. S1A).As a result, it was challenging to distinguish between the three layers in terms of their structure and boundaries based on visual inspection. To accurately depict the variation in Mg element distribution within the multi-gradient structure of the MgO/$MgCO_3$/PCL membrane, EDS analysis and mapping were conducted to each layer in each set of MgO/$MgCO_3$/PCL membrane to discern the disparities in Mg element distribution. Our results demonstrated a gradual decrease in Mg elemental proportion from the inner to the outer layers (Fig. S1B–D).

The morphologies of the MgO/$MgCO_3$/PCL membrane were also examined via SEM at the 4-week timepoint. Our results confirmed that, the fibers experienced partial collapse along with the degradation of materials, leading to a reduction in membrane thickness. Simultaneously, the fibers gradually dissolved and became finer, while the surface was coated with an abundance of corrosion products. Within a period of 4 weeks, the 10% MgO/$MgCO_3$/PCL group exhibited the highest weight-loss percentage, indicating an enhanced material degradation and subsequent release of Mg^{2+} (Fig. S2).

In vitro cell culture was conducted on the surface of the MgO/$MgCO_3$/PCL membrane to further assess the biocompatibility of the material. SEM analysis and Live/dead staining were performed. Our findings indicated that the morphology of PC12 cells and RSC96 cells was similar when cultured on PCL and three different compositions of MgO/$MgCO_3$/PCL membranes (10%, 20%, 30%), demonstrating their biocompatibility in terms of cell adhesion and cell growth in vitro. Live/dead staining also conformed no significant difference among four groups in terms of cytotoxicity (Fig. S3). Overall, the biological safety of the material was confirmed.

RSC96 cells were also cultured for 7 days and assessed using SEM to effectively illustrate an influence of the MgO/$MgCO_3$/PCL membrane on cell growth. Additionally, the impact of material extracts from different groups was quantified through CCK8 assay. Our findings validated the role of Mg^{2+} release from the MgO/$MgCO_3$/PCL membrane in promoting cellular proliferation. Notably, the 10% MgO/$MgCO_3$/PCL group exhibited superior cell growth, consistent with the sustained release profile of Mg^{2+} from the material (Fig. S4).

The surface properties of the MgO/$MgCO_3$/PCL multi-gradient nanofiber membrane were further characterized by measuring the contact angles of the four groups of materials. The mean contact angles of the membranes were $124.9° \pm 0.52°$ in the control group (PCL), $122.1° \pm 1.61°$ in the 10% MgO/$MgCO_3$/PCL group, $120.2° \pm 2.13°$ in the 20% MgO/$MgCO_3$/PCL group, and $120.9° \pm 2.53°$ in the 30% MgO/$MgCO_3$/PCL group (Fig. 1E). The findings revealed no statistically significant variances in contact angles across the materials, indicating comparable levels of interaction between the membrane surface and the test liquids. This further substantiated that the bioactive material primarily facilitated peripheral nerve regeneration by the release of Mg^{2+} rather than its physical properties.

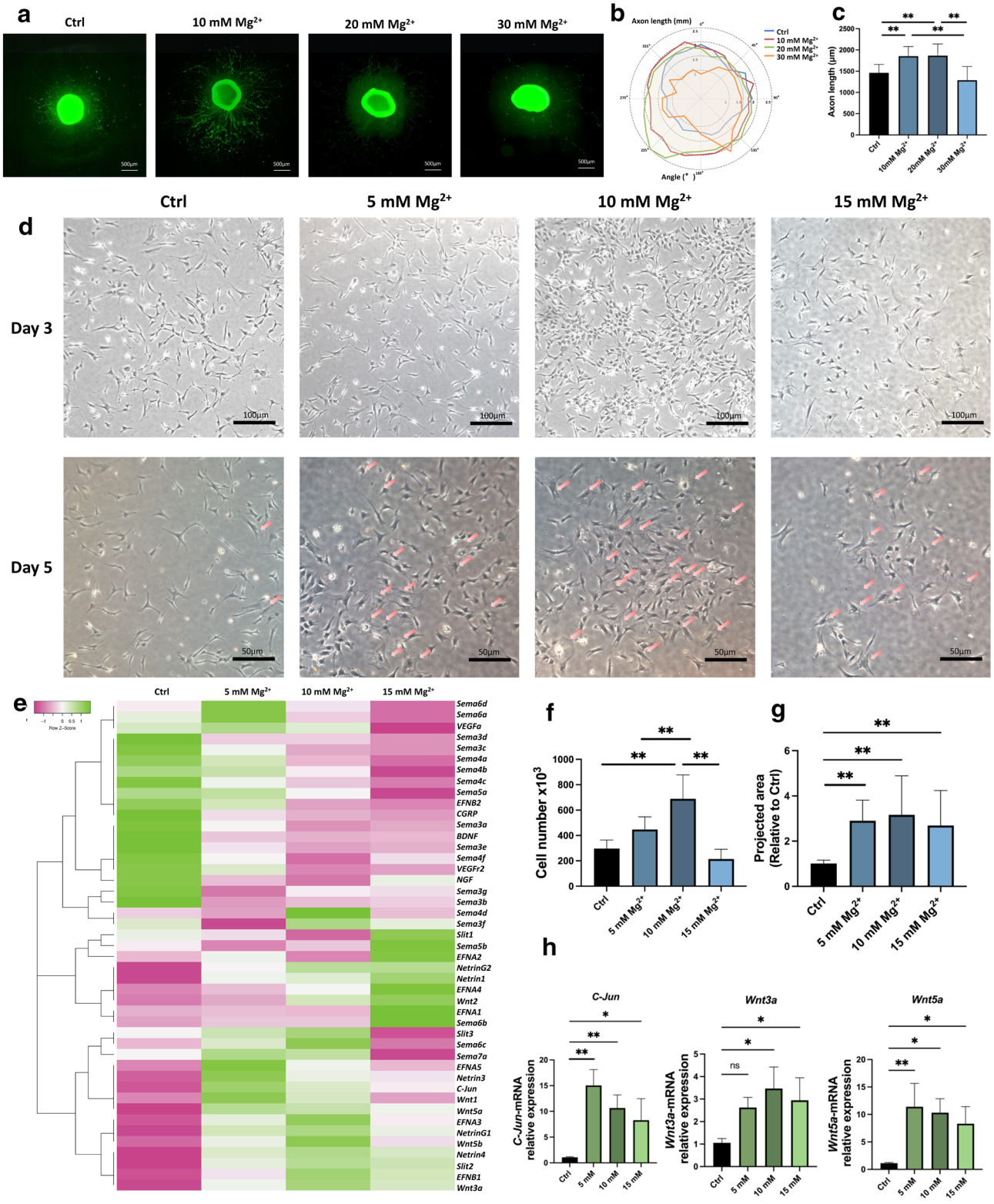
a
Ctrl
10 mM Mg2+
20 mM Mg2+
30 mM Mg2+
500μm
b
Axon length (mm)
Ctrl
10 mM Mg2+
20 mM Mg2+
30 mM Mg2+
Angle (°)
c
Axon length (μm)
Ctrl
10mM Mg2+
20mM Mg2+
30mM Mg2+
d
Ctrl
5 mM Mg2+
10 mM Mg2+
15 mM Mg2+
Day 3
Day 5
100μm
50μm
e
Ctrl
5 mM Mg2+
10 mM Mg2+
15 mM Mg2+
Row Z-Score
Sema6d
Sema6a
VEGFa
Sema3d
Sema3c
Sema4a
Sema4b
Sema4c
Sema5a
EFNB2
CGRP
Sema3a
BDNF
Sema3e
Sema4f
VEGFr2
NGF
Sema3g
Sema3b
Sema4d
Sema3f
Slit1
Sema5b
EFNA2
NetrinG2
Netrin1
EFNA4
Wnt2
EFNA1
Sema6b
Slit3
Sema6c
Sema7a
EFNA5
Netrin3
C-Jun
Wnt1
Wnt5a
EFNA3
NetrinG1
Wnt5b
Netrin4
Slit2
EFNB1
Wnt3a
f
Cell number x10^3
Ctrl
5 mM Mg2+
10 mM Mg2+
15 mM Mg2+
g
Projected area (Relative to Ctrl)
h
C-Jun
Wnt3a
Wnt5a
C-Jun-mRNA relative expression
Wnt3a-mRNA relative expression
Wnt5a-mRNA relative expression
ns

◂**Fig. 2** Effect of additional Mg^{2+} on DRG neurite growth and Schwann cell proliferation and phenotype conversion. **a** Primary DRG cell culture treated with varying Mg^{2+} concentrations (Ctrl, 10, 20, and 30 mM Mg^{2+}). **b** Demonstration of neurite outgrowth in different groups. **c** Longest axon length calculated every 15° in each direction ($n=4$); **d** Schwann cells supplemented with Mg^{2+} exhibited enhanced morphological extensions and significantly increased cell area over time. **e** Gene expression heatmap of axon guidance molecules, neurotrophic factors, the Wnt family, and C-Jun ($n=3$). **f** Cell number statistics. **g** Statistics of adhesion areas seen on cell morphological examination. **h** Gene expression of C-Jun, Wnt3a, and Wnt5a (compared to mRNA levels in the Ctrl group; $n=3$ *per* group). Data were expressed as the mean ± SD. Statistical analysis was performed using one-way ANOVA and Tukey's post-hoc test. $^{*}P<0.05$; $^{**}P<0.01$

3.3 Mg-Induced Neurite Outgrowth in Primary DRG Cultures

Previous studies have confirmed the safety and efficacy of Mg^{2+} in facilitating nerve regeneration. However, the specific signaling pathways and mechanisms by which Mg-encapsulated nerve scaffolds modulate the repair of peripheral nerve defects are still not thoroughly understood. Therefore, subsequent investigations were conducted using in vitro experiments to further clarify these mechanisms. We used primary rat DRG tissue cultures to examine the role of Mg^{2+} in promoting neurite outgrowth and determine the optimal concentration of Mg^{2+} required for this process. Consequently, we observed that Mg^{2+} induced neurite outgrowth in a dose-dependent manner. The length of DRG neurites in four groups (Ctrl, 10, 20, and 30 mM Mg^{2+}) was manually quantified after 5 days of incubation (Fig. 2A). The maximum distance of neurite extension was measured every 15° in each direction, with $n=4$ DRGs in each group (Fig. 2B). The average neurite extension in the four groups was 1461.63 ± 197.51 μm in the control group, 1856.24 ± 224.42 μm in the 10 mM Mg^{2+} group, 1867.35 ± 273.94 μm in the 20 mM Mg^{2+} group, and 1287.40 ± 324.93 μm in the 30 mM Mg^{2+} group (Fig. 2C). Compared to the control group, DRGs treated with both 10 mM and 20 mM Mg^{2+} demonstrated significantly longer neurite extensions. Additionally, Mg^{2+} enhanced the directional migration of Schwann cells toward axonal growth, suggesting that Mg^{2+} might enhance the interaction between Schwann cells and neuronal axons.

3.4 Mg^{2+} Facilitated Primary Schwann Cell Proliferation and Phenotype Conversion

Schwann cells, as the pivotal functional cells in peripheral nerve regeneration following injury, play a dominant role in orchestrating the entire course of nerve repair and regeneration [49]. This includes maintaining an optimal microenvironment for axonal regrowth, guiding the recovery of axonal regeneration, and facilitating the reinnervation of target organs [50]. The limited proliferative capacity and functionality of Schwann cells within the nerve scaffold are crucial factors contributing to suboptimal outcomes in nerve defect repairs [51]. Following nerve injury, Schwann cells undergo demyelination and transition to a reparative phenotype known as reparative Schwann cells (rSCs) [19]. These rSCs initiate nerve regeneration by secreting neurotrophic factors, clearing damaged myelin debris, and interacting with other cell types to maintain an environment conducive to successful regeneration [52]. Multiple signaling pathways, such as the mitogen-activated protein kinase (MAPK) pathway [53], are involved in regulating this phenotypic switch, with C-Jun serving as a critical transcription factor governing phenotype switching [34].

Primary rat Schwann cell cultures were employed to elucidate the impact of Mg^{2+} on the proliferation and phenotypic transition of Schwann cells (Fig. 2D). Our results demonstrated that Mg^{2+} could facilitate concentration-dependent increases in the proliferation of Schwann cells, with a significant rise observed in the 10 mM Mg^{2+} group (Fig. 2F). Over time, Schwann cells in the experimental group supplemented with Mg^{2+} exhibited enhanced morphological extensions and significantly increased cell area, indicative of the characteristic features associated with rSCs (Fig. 2G). The gene expression of axon guidance molecules (four families: netrins, slits, ephrins, and semaphorins) and neurotrophic factors (NGF, BDNF, and VEGF) were quantified by qPCR, and the mRNA expression levels of Sema4d, Sema6a, Netrin, Netrin3, Netrin4, NetrinG1, NetrinG2, and EFNA1 were higher in the experimental groups than the control groups (Fig. 2E). Quantitative PCR analysis revealed the significant up-regulated expression levels of key genes, including the transcriptional regulatory factors C-Jun and Wnt5a, in the experimental groups (Fig. 2H).

These results suggested that Mg^{2+} could stimulate a shift toward a reparative phenotype in Schwann cells, which served as the foundation for their proliferative capacity. During this process, Mg^{2+} up-regulated the expression levels of various axon-inducing factors. These results, combined with the primary DRG tissue culture results, suggested that Mg^{2+} could facilitate Schwann cell proliferation, migration, and phenotype conversion, which provided essential support and guidance for nerve regeneration by secreting neurotrophic factors and interacting with neurons. The Wnt signaling pathway might be an important mechanism influencing Schwann cell function during nerve regeneration.

3.5 CCK-8 Assay and Cell Scratch Assay in RSC96 Cell Cultures

RSC96 cell line cultures were used to further evaluate the optimal concentration of Mg^{2+}, its impact on Schwann cell

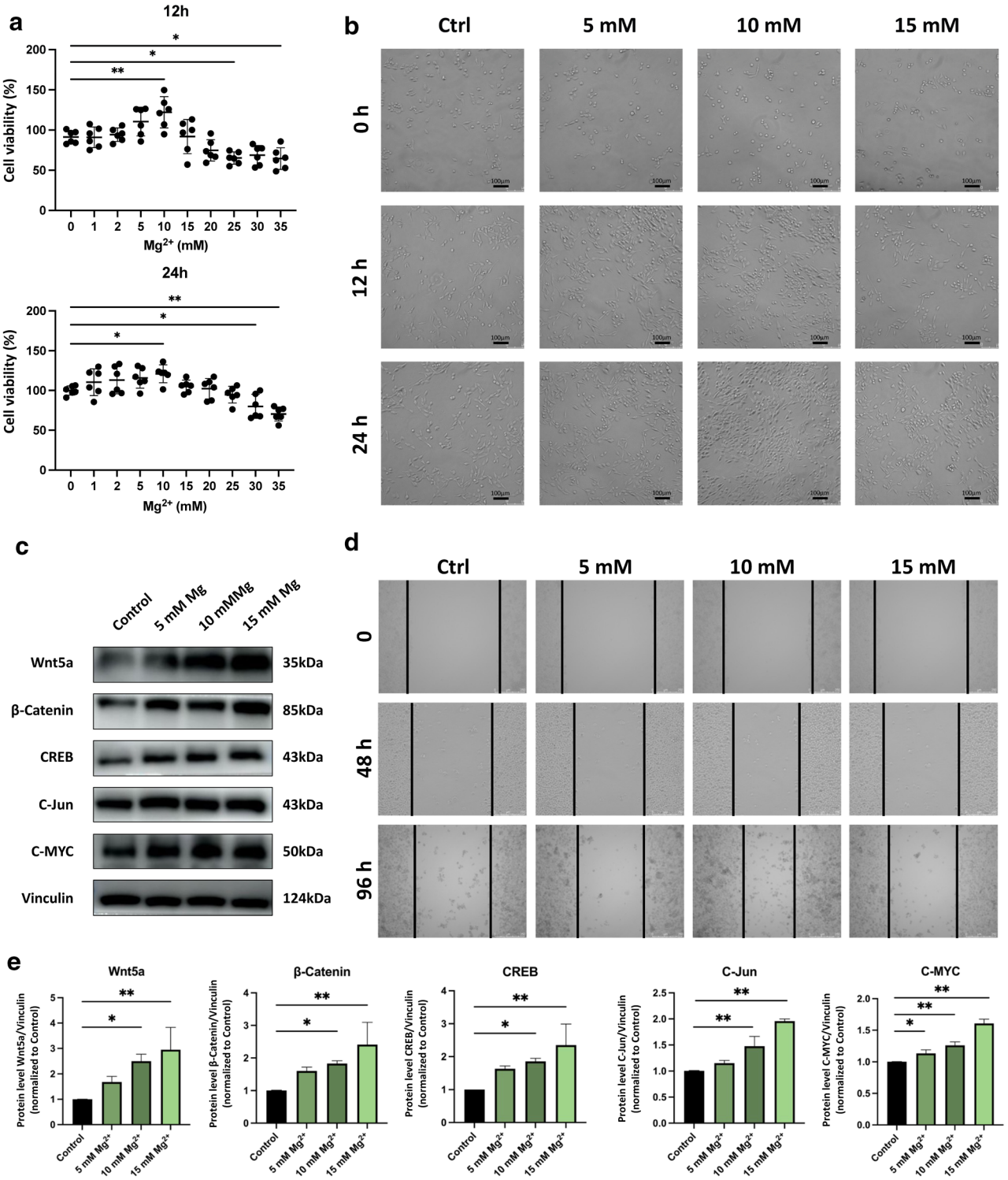

Fig. 3 Mg^{2+} increased Schwann cell proliferation and migration in RSC96 cell culture. **a** CCK-8 assay of cell viability and cell proliferation. **b** Mg^{2+} induced the proliferation of Schwann cells in a concentration-dependent manner. **c** Western blot results of Wnt5a, β-Catenin, CREB, C-Jun, and C-MYC. **d** Mg^{2+} induced the migration of Schwann cells in a concentration-dependent manner. **e** Normalized protein level of Wnt5a, β-Catenin, CREB, C-Jun and C-MYC. Data were expressed as the mean ± SD. Statistical analysis was performed using one-way ANOVA and Tukey's post-hoc test. $^{*}P < 0.05$; $^{**}P < 0.01$

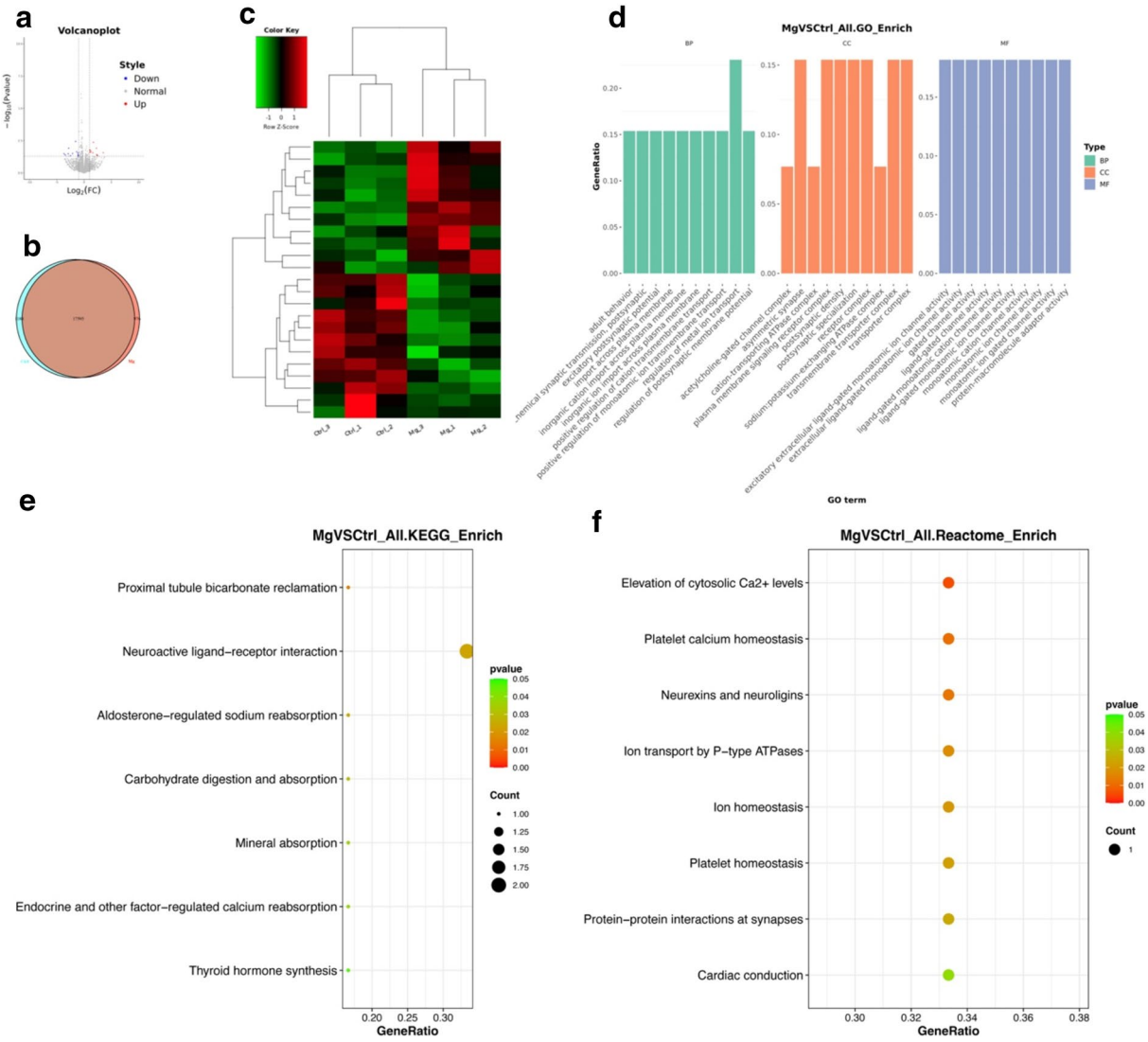

Fig. 4 Transcriptome sequencing of Mg^{2+}-induced peripheral nerve regeneration. **a** Volcano plot of differentially expressed genes. **b** Venn diagram of gene numbers. **c** Cluster analysis of differentially expressed genes. **d** GO functional enrichment analysis. **e** KEGG functional enrichment analysis. **f** Reactome enrichment analysis

proliferation and migration, and changes in protein levels. Compared to primary rat Schwann cell culture, this provided a more convenient culture system for our study. CCK-8 and cell scratch assays were conducted. The CCK-8 cell proliferation assay demonstrated that Mg^{2+} effectively stimulated the proliferation of Schwann cells in a concentration-dependent manner (Fig. 3A). As the concentration of Mg^{2+} increased, cell proliferation was progressively enhanced, with a significant increase observed in the 10 mM group, which represented the optimal concentration. However, when the concentration exceeded 10 mM, the promotion of proliferation gradually weakened, and concentrations greater than 20 mM inhibited Schwann cell proliferation to some extent (Fig. 3B). The scratch assay results indicated that Mg^{2+} facilitated Schwann cell migration. The results of the cell scratch assay indicated that 10 mM Mg^{2+} treatment significantly enhanced the migratory capacity of Schwann cells (Fig. 3D).

The qPCR results obtained from primary Schwann cell cultures indicated that the Wnt signaling pathway could influence Schwann cell function during nerve regeneration. Subsequently, protein expression was further examined using western blot analysis to gain deeper insight into the underlying molecular mechanisms. Among the Wnt family, Wnt5a exhibited elevated protein expression levels, which were consistent with the qPCR results. Mg^{2+} treatment increased β-Catenin and CREB expression, indicating the potential involvement of the Wnt/β-Catenin signaling pathway in

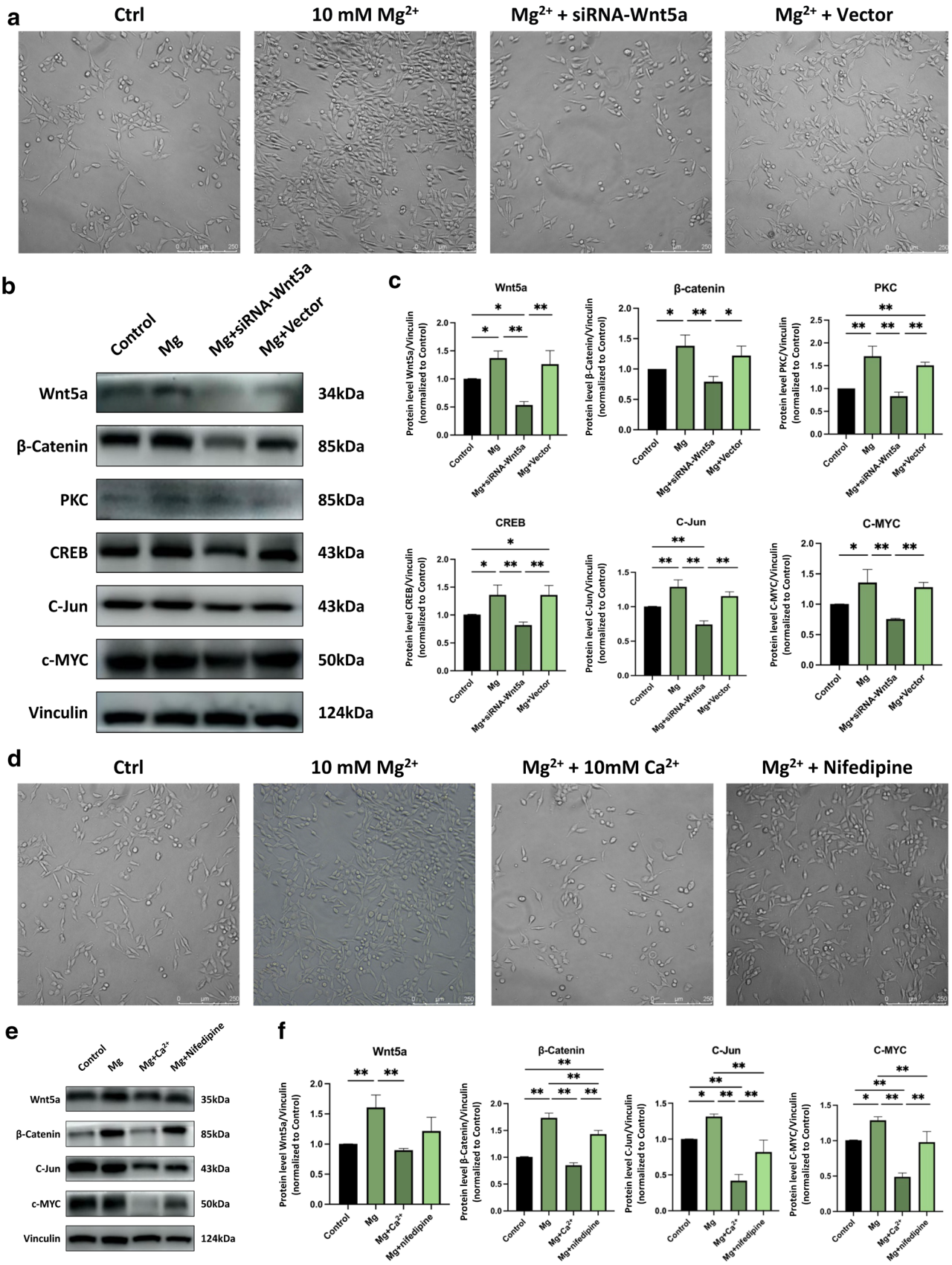
a
Ctrl
10 mM Mg2+
Mg2+ + siRNA-Wnt5a
Mg2+ + Vector
b
Control
Mg
Mg+siRNA-Wnt5a
Mg+Vector
Wnt5a
34kDa
β-Catenin
85kDa
PKC
85kDa
CREB
43kDa
C-Jun
43kDa
c-MYC
50kDa
Vinculin
124kDa
c
Wnt5a
β-catenin
PKC
CREB
C-Jun
C-MYC
Protein level Wnt5a/Vinculin (normalized to Control)
Protein level β-Catenin/Vinculin (normalized to Control)
Protein level PKC/Vinculin (normalized to Control)
Protein level CREB/Vinculin (normalized to Control)
Protein level C-Jun/Vinculin (normalized to Control)
Protein level C-MYC/Vinculin (normalized to Control)
d
Ctrl
10 mM Mg2+
Mg2+ + 10mM Ca2+
Mg2+ + Nifedipine
e
Control
Mg
Mg+Ca2+
Mg+Nifedipine
Wnt5a
35kDa
β-Catenin
85kDa
C-Jun
43kDa
c-MYC
50kDa
Vinculin
124kDa
f
Wnt5a
β-Catenin
C-Jun
C-MYC
Protein level Wnt5a/Vinculin (normalized to Control)
Protein level β-Catenin/Vinculin (normalized to Control)
Protein level C-Jun/Vinculin (normalized to Control)
Protein level C-MYC/Vinculin (normalized to Control)
Mg+nifedipine

◂**Fig. 5** Mg^{2+} regulated Schwann cells function by activating Wnt signaling. **a** RSC96 cultured cells treated with additional Mg^{2+}, Lipo:Wnt5a-siRNA, and Lipo:blank. **b** Protein expression levels of Wnt5a, β-catenin, PKC, CREB, c-Myc, and c-Jun in four groups (Ctrl, 10 mM Mg^{2+}, Mg^{2+} with Lipo:Wnt5a-siRNA, and Mg^{2+} with Lipo:blank); **c** Normalized protein level of Wnt5a, β-Catenin, PKC, CREB, C-MYC and C-Jun; **d** RSC96 cultured cells treated with additional Mg^{2+}, Ca^{2+}, and nifedipine. **e** Protein expression levels of Wnt5a, β-Catenin, C-MYC and C-Jun in four groups (Ctrl, 10 mM Mg^{2+}, 10 mM Mg^{2+} with 10 mM Ca^{2+}, and 10 mM Mg^{2+} with nifedipine). **f** Normalized protein level of Wnt5a, β-Catenin, C-MYC, and C-Jun. Data were expressed as the mean ± SD. Statistical analysis was performed using one-way ANOVA and Tukey's post-hoc test. $^{*}P < 0.05$; $^{**}P < 0.01$

cellular responses to Mg^{2+}. Furthermore, the up-regulation of C-MYC expression suggested that Mg^{2+} facilitated cellular proliferation. Lastly, the increased expression of C-Jun reflected the transition of Schwann cells to a repair phenotype as part of their response to nerve injury (Fig. 3C, E).

3.6 Transcriptome Sequencing of Mg^{2+}-Induced Peripheral Nerve Regeneration

Based on the data obtained from the experiments, we conducted a comprehensive screening of Mg-induced gene expression regulation through transcriptome sequencing. Total RNA was extracted from RSC96 cells in the control and 10 mM Mg^{2+} groups cultured for 72 h. The distribution of genes with differential expression between the two groups was displayed in a volcano plot. Genes with varying expression levels were identified by applying a threshold of $|\log2(\text{Foldchange})| > 1$ and $\text{padj} < 0.05$. Analysis of these genes resulted in blue and red Foldchange and padj values, indicating up-regulated and down-regulated genes respectively (Fig. 4A). A Venn diagram was used to illustrate overlapping gene expression among the groups, where each circle represented the total count of uniquely expressed genes, while the overlapping sections signified the genes shared between the groups (Fig. 4B). Cluster analysis was used to group similar samples and genes based on gene expression patterns. The map in Fig. 4C shows low expression in green and high expression in red, with lines indicating clustering outcomes. We used clusterProfiler to detect functional changes in differential genes, analyzing enriched GO entries for molecular functions, biological processes, and cellular components (Fig. 4D). The enriched pathways of differentially expressed genes in KEGG analysis were visualized, focusing on the top 20 genes with an adjusted P value of < 0.05. The red dots in Fig. 4E indicate higher significance. Reactome enrichment analysis was used to visualize the differentially expressed genes. A selected subset of the top 20 genes with P-adjusted results below 0.05 were presented, where the dot size represented the number of enriched differentially expressed genes (Fig. 4F).

Our findings indicated that Mg^{2+} treatment had a significant impact on intracellular calcium levels, leading to changes in the physiological responses of the cells. Exploring the interaction between these two ions could provide valuable insight into various cellular processes, such as muscle contraction, nerve signaling, and enzymatic activity. Although Wnt pathway activation was suggested by the cell experiments, this pathway did not show enrichment in the sequencing results. This discrepancy could be attributed to either the 72 h sample collection time or the small sample size. Nevertheless, the sequencing results can enhance our understanding of the regulatory role of Mg^{2+} in Schwann cells. The complete sequencing data appear in the Supplementary Material.

3.7 Mg^{2+} Regulated Schwann Cell Function by Activating Wnt Signaling

Wnt signaling plays a vital role in the peripheral nerve regeneration process [54] and regulates cell proliferation and differentiation through various mechanisms. Wnt protein plays a crucial role in controlling cell growth, development, and differentiation by activating the Wnt signaling pathway in target cells through paracrine action [55]. This pathway encompasses the canonical Wnt/β-Catenin signaling pathway [56] and the non-canonical Wnt/Ca^{2+} signaling pathway [57]. Recent studies have demonstrated the extensive involvement of the Wnt5a signaling pathway in the pathophysiological process of peripheral nerve injury, highlighting its regulatory role in nerve regeneration [58–60]. Wnt5a exerts regulatory effects on cell growth by activating the Wnt/β-Catenin pathway and initiating the Wnt/Ca^{2+} pathway by binding with frizzled (FZD) receptor. This interaction leads to G protein-mediated PLC activation and intercellular Ca^{2+} release, ultimately resulting in the activation of PKC and calmodulin-dependent protein kinase II (CaMKII) [61, 62].

We applied siRNA transfection in vitro to knock down Wnt5a and evaluate the proliferation of Schwann cells (four groups: Ctrl, 10 mM Mg^{2+}, Mg^{2+} with Lipo:Wnt5a-siRNA, Mg^{2+} with Lipo:blank) to further verify the regulation of the Wnt signaling pathway by Mg^{2+} in Schwann cells. The cellular morphology (Fig. 5A) and western blot results (Fig. 5B, C) showed that Wnt5a-siRNA significantly repressed cell proliferation compared to 10 mM Mg^{2+} without siRNA. The expression of Wnt5a, β-Catenin, CREB, C-MYC, and C-Jun were down-regulated by Wnt5a-siRNA, demonstrating that the Wnt/β-Catenin signaling pathway was activated. Based on previous research demonstrating the inhibitory effect of Mg^{2+} on Ca^{2+} influx, we hypothesized that Mg^{2+} might suppress the Wnt/Ca^{2+} pathway by attenuating Ca^{2+} influx, a commonly recognized negative regulatory mechanism. In our in vitro experiments, 10 mM Ca^{2+} treatment significantly

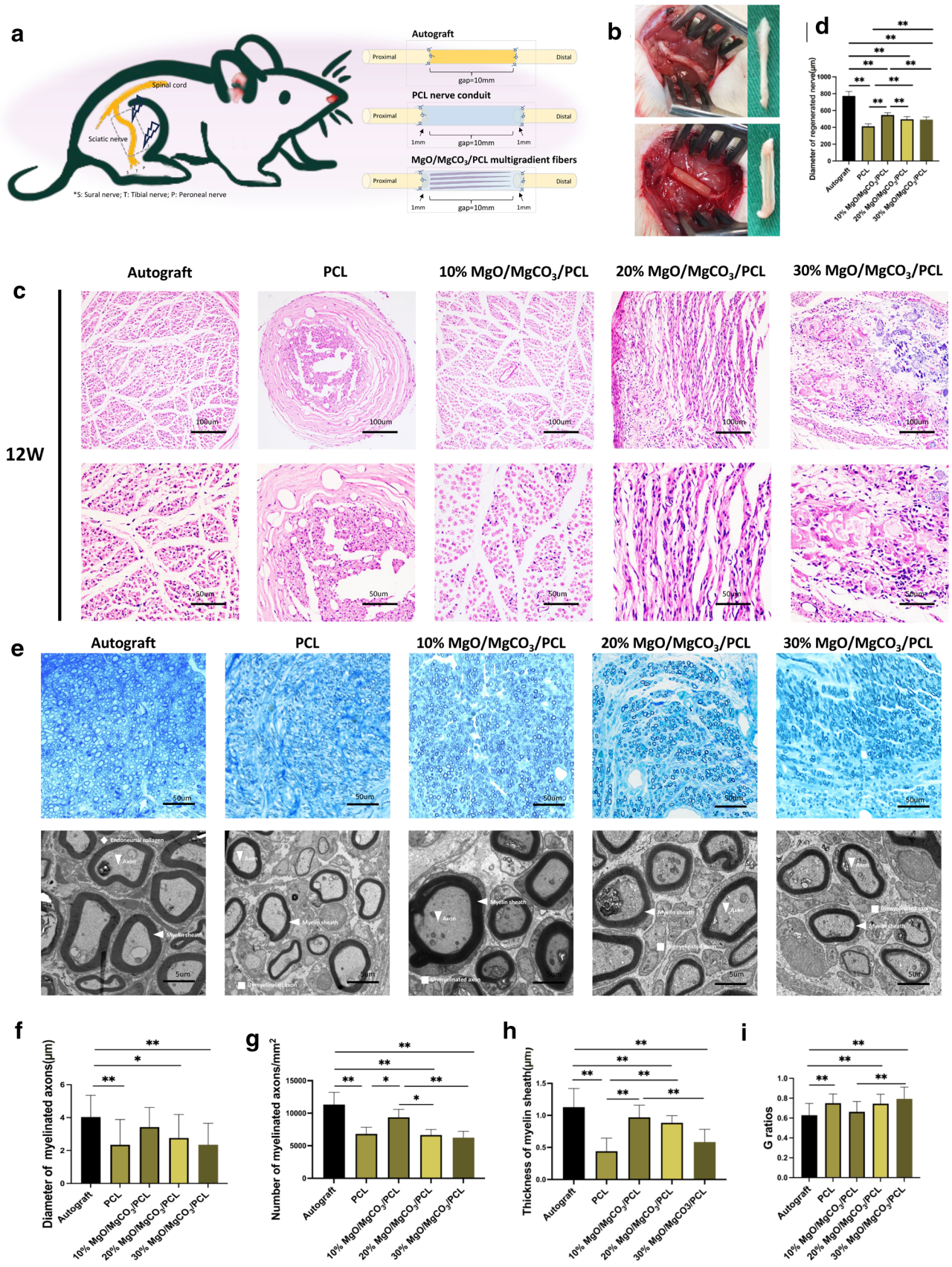
a
Spinal cord
Sciatic nerve
*S: Sural nerve; T: Tibial nerve; P: Peroneal nerve
Autograft
Proximal
Distal
gap=10mm
PCL nerve conduit
1mm
MgO/MgCO3/PCL multigradient fibers
b
d
Diameter of regenerated nerve(μm)
Autograft
PCL
10% MgO/MgCO3/PCL
20% MgO/MgCO3/PCL
30% MgO/MgCO3/PCL
c
12W
100um
50um
e
Endoneurial collagen
Axon
Myelin sheath
5um
f
Diameter of myelinated axons(μm)
g
Number of myelinated axons/mm2
h
Thickness of myelin sheath(μm)
i
G ratios

◂**Fig. 6** H&E analysis and remyelination of regenerated nerves. **a** Schematic illustration of animal surgery. **b** Harvested regenerated nerves. **c** H&E staining of the autograft, PCL nerve conduit, 10% MgO/$MgCO_3$/PCL, 20% MgO/$MgCO_3$/PCL, and 30% MgO/$MgCO_3$/PCL groups. **d** Diameter of the regenerated nerves (μm) ($n = 4$). **e** Toluidine blue staining of transverse sections of harvested grafts 12 weeks after surgery and TEM analysis of remyelinated axons. **f** Diameter of the myelinated axons (μm) ($n = 5$). **g** Number of myelinated axons ($n = 5$). **h** Thickness of the new myelin sheath (μm) ($n = 5$). **i** G-ratio ($n = 5$). Data were analyzed by one-way ANOVA followed by Tukey's post hoc test and expressed as the mean ± SD $^*P < 0.05$; $^{**}P < 0.01$

inhibited cellular proliferation and attenuated downstream effectors (four groups: Ctrl, 10 mM Mg^{2+}, 10 mM Mg^{2+} with 10 mM Ca^{2+}, and 10 mM Mg^{2+} with nifedipine). This inhibitory effect was reversible by the administration of nifedipine (a calcium channel blocker) (Fig. 5D). The western blot results confirmed that the expression of Wnt5a, β-Catenin, C-MYC, and C-Jun was down-regulated by additional Ca^{2+} (Fig. 5E, F), indicating that Mg^{2+} could suppress the Wnt/Ca^{2+} signaling pathway.

3.8 H&E Staining and Immunohistochemical Analysis of Regenerated Nerves

A 10 mm sciatic nerve defect model was established in SD rats to evaluate the materials in vivo. The rats were randomly allocated to one of five groups: autograft, PCL nerve conduit, 10% MgO/$MgCO_3$/PCL, 20% MgO/$MgCO_3$/PCL, and 30% MgO/$MgCO_3$/PCL. The autograft group served as the positive control. For the experimental groups, multi-gradient nanofiber membranes composed of MgO/$MgCO_3$/PCL were fabricated into fibers measuring 0.5 mm × 12 mm and implanted into 3D-engineered PCL nerve conduits (Fig. 6A, Fig. S5). Six weeks after surgery, nerve continuity was observed to be restored. Regenerated nerve tissue could be seen in the nerve conduit of the experimental group (Fig. 6B). The middle segment of nerve samples, 2 mm long, collected 6 and 12 weeks post-surgery, was subjected to histological assessment for regenerated nerves. H&E staining was applied to evaluate the newly formed nerve fibers in each experimental group, and measurements of the diameters of newly formed nerves on transverse sections were taken (Fig. 6C, S6). The autograft group exhibited the most significant size with statistical significance, followed by the 10% MgO/$MgCO_3$/PCL, 20% MgO/$MgCO_3$/PCL, 30% MgO/$MgCO_3$/PCL, and the PCL nerve conduit (Fig. 6D). The results indicated that the nerve repair efficacy of the three groups implanted with MgO/$MgCO_3$/PCL multi-gradient nanofiber was significantly superior to that of the negative control group (PCL nerve conduit). However, among the three experimental groups, the 10% MgO/$MgCO_3$/PCL group, which had the lowest concentration of Mg^{2+}, exhibited the most favorable repair effect. Indeed, during the initial 6 weeks of nerve regeneration, the 10% MgO/$MgCO_3$/PCL group exhibited a higher rate of effective Mg^{2+} release, as previously mentioned. Conversely, while it was hypothesized that both the 20% MgO/$MgCO_3$/PCL and 30% MgO/$MgCO_3$/PCL groups might continue releasing for more than 8 weeks, they did not show repair effects better than the 10% MgO/$MgCO_3$/PCL group. Moreover, according to our findings, significant inflammatory responses were observed in the 30% MgO/$MgCO_3$/PCL group. Hence, whether an overabundance of Mg^{2+} might confer an unfavorable effect on nerve regeneration in our experimental scenario could not be ruled out.

To assess the impact of Mg^{2+} on Schwann cell phenotypic conversion in vivo, immunohistochemistry was utilized to evaluate the expression of C-Jun protein in nerve samples at 6 weeks. The findings indicated that, compared to the negative control (PCL) group, the three groups containing MgO/$MgCO_3$/PCL fibers were able to modulate the transformation of SCs towards a reparative phenotype through sustained release of Mg^{2+} (Fig. S7).

3.9 Remyelination of Regenerated Nerves

Regenerated nerve remyelination was assessed using toluidine blue staining and TEM analysis (Fig. 6E). Nerve graft samples were collected 12 weeks post-surgery, with cross-sectional examination focusing on the distal 2 mm segments of the regenerated nerves. The diameter and quantity of myelinated axons were evaluated in TEM images (Fig. 6F, G), as well as the thickness of the new myelin sheath (Fig. 6H). Additionally, the G-ratio was calculated to gauge the maturity of the myelinated axons (Fig. 6I). Among the five groups investigated, superior remyelination was observed in the autograft group and characterized by distinct, thick, and electron-dense myelin sheaths surrounding regenerated axons. Consistent with the H&E analysis findings, the 10% MgO/$MgCO_3$/PCL group demonstrated significantly enhanced remyelination in terms of both the quantity and size of the myelinated axons, as well as the thickness of the newly formed myelin sheath compared to the 20% MgO/$MgCO_3$/PCL, 30% MgO/$MgCO_3$/PCL, and PCL nerve conduit groups. Furthermore, in the 20% MgO/$MgCO_3$/PCL group, the thickness of the new myelin sheath exhibited a significant improvement compared to both the 30% MgO/$MgCO_3$/PCL and the PCL nerve conduit groups. However, no significant differences in diameter, the quantity of myelinated axons, or the G-ratio were observed between the 20% MgO/$MgCO_3$/PCL, 30% MgO/$MgCO_3$/PCL, and PCL nerve conduit groups. These findings suggest that Mg^{2+} played a significant role in facilitating axonal myelination. While Schwann cells were primarily responsible for the myelination process, the sustained release of

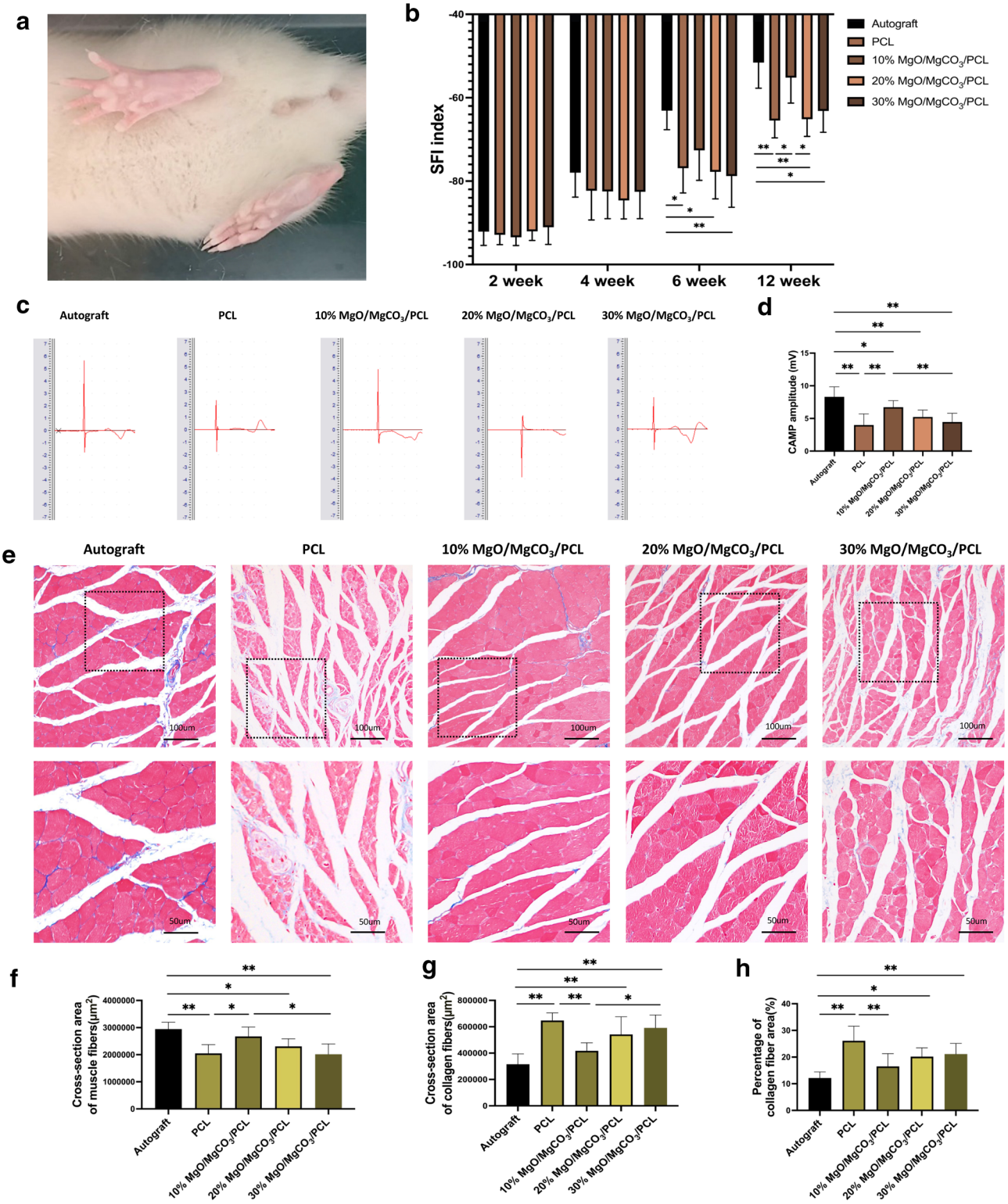

Fig. 7 Functional recovery analysis assessed using SFI values, electrophysiological assessment, and Masson's staining of transverse sections of the triceps surae muscle. **a** Demonstration of SFI value calculation. **b** SFI values gradually increased over time in all groups, demonstrating the partial restoration of function 6 and 12 weeks post-surgery ($n=5$). **c** CAMP amplitude of the five groups at 12 weeks post-surgery. **d** CAMP amplitude in mV ($n=4$). **e** Masson's staining of the triceps surae muscle samples 12 weeks post-surgery. **f** Cross-sectional area of muscle fibers. **g** Cross-sectional area of collagen fibers. **h** Percentage of collagen fiber area ($n=4$). Data are expressed as the mean ± SD. Statistical analysis was performed by one-way ANOVA and Tukey's post-hoc

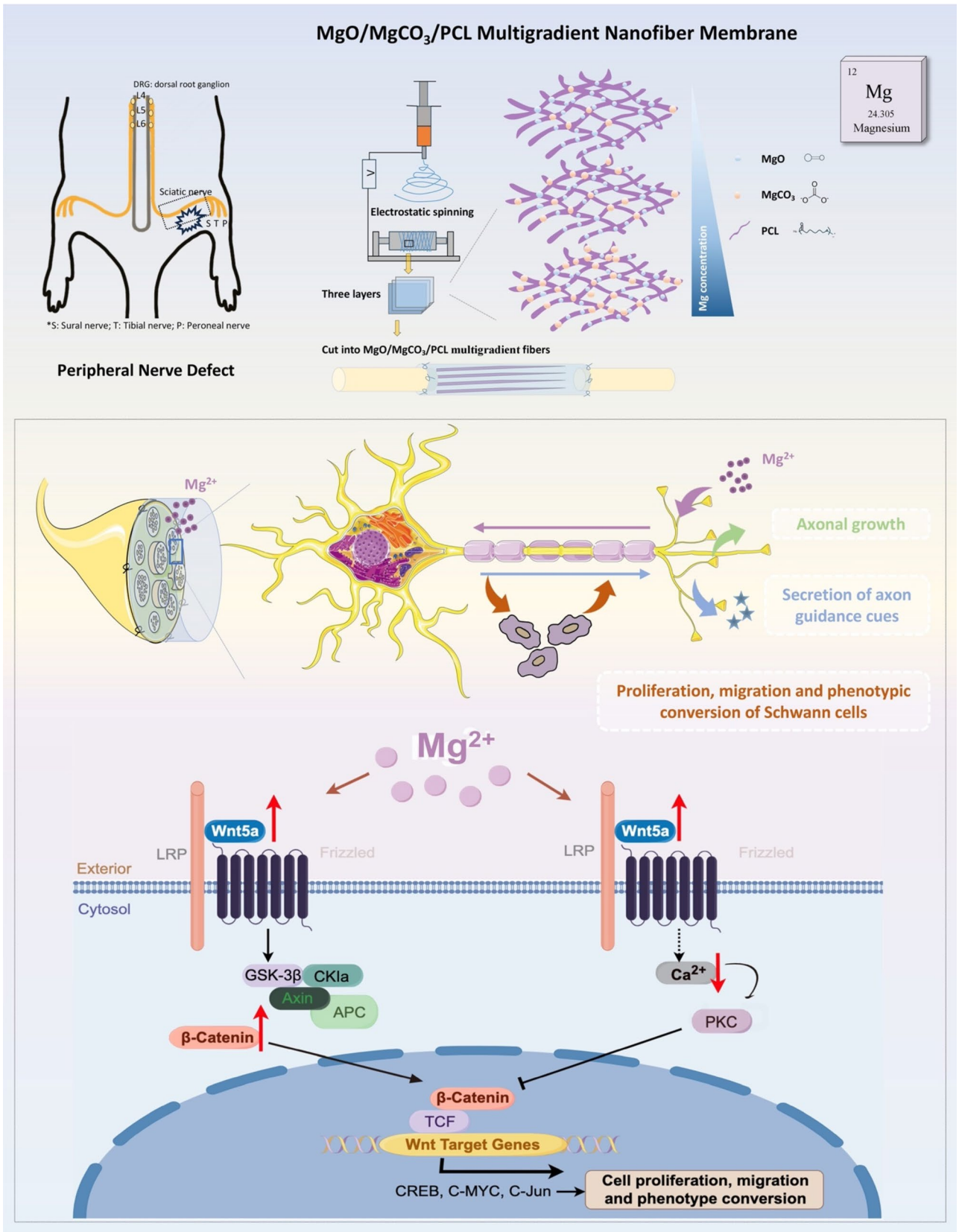

Fig. 8 Schematic illustration of bioactive $MgO/MgCO_3$/PCL multi-gradient fibers facilitating peripheral nerve regeneration by regulating Schwann cell function and activating the Wnt signaling pathway

Mg^{2+} from the MgO/$MgCO_3$/PCL multi-gradient fibers might impact the functionality of Schwann cells during the intermediate and late stages of nerve regeneration. Maintaining an optimal balance of Mg^{2+} is essential for supporting Schwann cell function and promoting efficient nerve regeneration.

3.10 Functional Evaluation of Nerve Regeneration

Paw prints were captured 2, 4, 6 and 12 weeks post-surgery to evaluate the functional recovery of the peripheral nerve (Fig. 7A, B). SFI, which is a well-established and sophisticated method for assessing sciatic nerve function in rats, was calculated, providing a non-invasive approach to evaluate the extent of motor function recovery in target muscles following injury to the sciatic nerve or its branches. SFI values ranged from 0, which represented a normal value, to − 100, which indicated complete nerve transection. A lower absolute SFI value suggests better recovery of nerve function. Rats in all five experimental groups showed some improvement in overall motor function over time. Consistent with previous research, the autograft group had the lowest absolute SFI value among the five groups, followed by the 10% MgO/$MgCO_3$/PCL group. No statistically significant differences between the remaining three groups were observed.

Electrophysiological assessment was performed 12 weeks post-surgery. CMAPs were recorded by placing the signal-receiving electrode at the triceps surae muscles in five groups. The autograft group demonstrated the highest amplitudes of compound muscle action potential (CMAP), followed by the 10% HA-10% MgO/$MgCO_3$/PCL group. There were no statistically significant differences among the remaining three groups (Fig. 7C, D).

3.11 Evaluation of Reinnervated Triceps Surae Muscles

Following nerve damage, muscle atrophy was observed in the affected triceps surae muscles in all five groups, and improvement in reinnervation was demonstrated over time. Triceps surae muscle samples were collected 12 weeks post-surgery for Masson's trichrome staining to evaluate muscle structure (Fig. 7E). The autograft group showed the best results among the five experimental groups, with an increase in the muscle fiber cross-sectional area, a decrease in the collagen fiber area, and a decreased percentage of collagen fiber area. Among the other four groups, the 10% MgO/$MgCO_3$/PCL group had the largest muscle fiber cross-sectional area, the greatest reduction in the collagen fiber area and lowest percentage of collagen fiber area. However, no significant differences were observed among the 20% MgO/$MgCO_3$/PCL, 30% MgO/$MgCO_3$/PCL, and PCL nerve conduit groups. The average percentage of collagen fiber area in the five groups was 12.2% ± 2.3% in the autograft group, 26.1% ± 5.5% in the PCL group, 16.5% ± 4.7% in the 10% MgO/$MgCO_3$/PCL group, 20.1% ± 3.3% in the 20% MgO/$MgCO_3$/PCL group, and 21.1% ± 4.0% in the 30% MgO/$MgCO_3$/PCL group (Fig. 7F–H).

Overall, our findings indicated that the development of a tunable and effective Mg^{2+} release system was crucial for enhancing the efficacy of Mg^{2+}-encapsulated nerve scaffolds in peripheral nerve injury. This MgO/$MgCO_3$/PCL multi-gradient fibers system had the potential to modulate the local microenvironment of nerve regeneration, facilitate axonal regrowth, improve Schwann cell function, and ultimately promote motor function recovery.

The study's limitation lies in the lack of in vivo investigations into the mechanism by which Mg^{2+} promoted Schwann cell function. Furthermore, the nerve conduit used in this study had a relatively simplistic structure. Lastly, due to the limitations of experimental techniques, we were not able to detect the actual concentration of Mg^{2+} in the local regeneration microenvironment, thus the optimal therapeutic concentration of Mg^{2+} in vivo remained unclear. In our study, the concentration of Mg^{2+} released by MgO/$MgCO_3$/PCL fibers might not necessarily be the optimal therapeutic concentration of Mg^{2+} in vivo.

Future research should explore incorporating drugs, cells, and other active ingredients into the material to further enhance the therapeutic efficacy of Mg^{2+}-encapsulated nerve scaffolds [1, 49, 63]. Our study provided new insights into the regulatory role of Mg^{2+} in the Wnt pathway during peripheral nerve regeneration (Fig. 8), revealing the molecular mechanisms involved in promoting peripheral nerve repair using Mg^{2+}-encapsulated nerve scaffolds. The findings established a solid theoretical foundation for future applications and clinical translation.

4 Conclusions

In this study, we used electrospinning technology to develop multi-gradient nanofiber membranes composed of MgO/$MgCO_3$/PCL for the tunable release of Mg^{2+}, which was regulated for over a period of 6 weeks, depending on the concentration of the Mg monomer. The in vivo implantation of these multi-gradient fibers to repair a 10-mm sciatic nerve defect in rats suggested their ability to promote peripheral nerve regeneration and motor function recovery. The controlled release of Mg^{2+} during the middle and late stages of nerve regeneration facilitated the myelination process in regenerating axons. Additionally, the potential mechanisms by which Mg^{2+}-induced proliferation, migration, and transition to a repair phenotype occur in Schwann cells were

discussed. The Wnt signaling pathway was identified as an important mechanism influencing Schwann cell function during nerve regeneration. The novel multi-gradient controlled-released magnesium-based nerve scaffold designed in this study had advantages such as low preparation cost, high efficiency, wide adaptability, and strong compatibility. These findings highlight the significant application potential of magnesium-containing biomaterials in treating nervous system diseases and lay a solid theoretical foundation for future applications and clinical translation.

Supplementary Information The online version contains supplementary material available at https://doi.org/10.1007/s42765-024-00489-3.

Acknowledgements ZY, ZYC, and XH contributed equally to this study. This work was financially supported by the National Key R&D Program of China (2022YFB3808000), the National Natural Science Foundation of China (82402802, 82404113, 82302713, U23A20490), the China Postdoctoral Science Foundation (2023M742390), the Guangdong Basic and Applied Basic Research Foundation (2022A1515012663, 2023A1515220250, 2023A1515111068), the Shenzhen Science and Technology Innovation Program (RCBS20231211090537061, JCYJ20230807095203007, JCYJ20230807095121041), the Shenzhen Key Medical Discipline Construction Fund (SZXK023), the Sanming Project of Medicine in Shenzhen (SZSM202211038), the Shenzhen High-level Hospital Construction Fund, and the Scientific Research Foundation of Peking University Shenzhen Hospital (LCYJZD2021005, KYQD2023244, KYQD2023245). The authors also gratefully acknowledged the kindly financial support provided by the Youth Talent Support Program of the China Association for Science and Technology, and the Top Young Talents of Foal Eagle Program of Fujian Province to Jin Zhang.

Author Contributions Conceptualization: ZY, YL, JZ, and DLW. Methodology: ZY, ZYC, YL, LLL, XH, YHW, SXH, QZ, LLS, and LJM. Investigation: ZY, ZYC, XH, and YL. Visualization: YHW, LLS, LJM, and SEL. Funding acquisition: ZY, ZYC, JZ, DLW, and YL. Project administration: ZY, YL, JZ, and DLW. Supervision: DLW, YL, JZ, and LXX. Writing – original draft: ZY, ZYC, and XH. Writing – review & editing: LXX, SNF, DLW, JZ, and YL.

Data availability The data that support the findings of this study are available from the corresponding author upon reasonable request.

Declarations

Conflict of Interest The authors have no conflicts of interest to declare.

References

1. Zhou W, Rahman MSU, Sun C, Li S, Zhang N, Chen H, Han CC, Xu S, Liu Y. Perspectives on the novel multifunctional nerve guidance conduits: from specific regenerative procedures to motor function rebuilding. *Adv Mater*. **2024**;*36*:e2307805.
2. Richards JT, Baird MD, Tintle SM, Souza JM, Renninger CH, Potter BK. Peripheral nerve management in extremity amputations. *Orthop Clin North Am*. **2022**;*53*:155.
3. Gong B, Zhang X, Zahrani AA, Gao W, Ma G, Zhang L, Xue J. Neural tissue engineering: from bioactive scaffolds and in situ monitoring to regeneration. *Exploration*. **2022**;*2*:20210035.
4. Liu J, Song Q, Yin W, Li C, An N, Le Y, Wang Q, Feng Y, Hu Y, Wang Y. Bioactive scaffolds for tissue engineering: a review of decellularized extracellular matrix applications and innovations. *Exploration*. **2024**, 20230078.
5. Gu X, Ding F, Williams DF. Neural tissue engineering options for peripheral nerve regeneration. *Biomaterials*. **2014**;*35*:6143.
6. Xia B, Gao X, Qian J, Li S, Yu B, Hao Y, Wei B, Ma T, Wu H, Yang S, Zheng Y, Gao X, Guo L, Gao J, Yang Y, Zhang Y, Wei Y, Xue B, Jin Y, Luo Z, Zhang J, Huang J. A novel superparamagnetic multifunctional nerve scaffold: a remote actuation strategy to boost in situ extracellular vesicles production for enhanced peripheral nerve repair. *Adv Mater*. **2024**;*36*:e2305374.
7. Yang Y, Yin X, Wang H, Qiu W, Li L, Li F, Shan Y, Zhao Z, Li Z, Guo J, Zhang J, Zhao Y. Engineering a wirelessly self-powered and electroconductive scaffold to promote peripheral nerve regeneration. *Nano Energy*. **2023**;*107*:108145.
8. Ye L, Xu J, Mi J, He X, Pan Q, Zheng L, Zu H, Chen Z, Dai B, Li X, Pang Q, Zou L, Zhou L, Huang L, Tong W, Li G, Qin L. Biodegradable magnesium combined with distraction osteogenesis synergistically stimulates bone tissue regeneration via CGRP-FAK-VEGF signaling axis. *Biomaterials*. **2021**;*275*:120984.
9. He X, Li Y, Miao H, Xu J, Ong MT-y, Wang C, Zheng L, Wang J, Huang L, Zu H, Yao Z, Mi J, Dai B, Li X, Yung PS-h, Yuan G, Qin L. High formability Mg-Zn-Gd wire facilitates ACL reconstruction via its swift degradation to accelerate intra-tunnel endochondral ossification. *J Magnes Alloy*. **2024**, *12*:295.
10. Nabiyouni M, Bruckner T, Zhou H, Gbureck U, Bhaduri SB. Magnesium-based bioceramics in orthopedic applications. *Acta Biomater*. **2018**;*66*:23.
11. Zhang J, Zhang B, Zhang J, Lin W, Zhang S. Magnesium promotes the regeneration of the peripheral nerve. *Front Cell Dev Biol*. **2021**;*9*:717854.
12. Cai Y, Chen Y, Zhang G, Lin Y, Zhang J, Liang J, Lv L, Wang Y, Fang X, Dang X. The GDNF-gel/HA-Mg conduit promotes the repair of peripheral nerve defects by regulating PPAR-gamma/RhoA/ROCK signaling pathway. *iScience*. **2024**, *27*, 108969.
13. Monfared A, Ghaee A, Ebrahimi-Barough S. Fabrication of tannic acid/poly(N-vinylpyrrolidone) layer-by-layer coating on Mg-based metallic glass for nerve tissue regeneration application. *Colloids Surf B Biointerfaces*. **2018**;*170*:617.
14. Vennemeyer JJ, Hopkins T, Hershcovitch M, Little KD, Hagen MC, Minteer D, Hom DB, Marra K, Pixley SK. Initial observations on using magnesium metal in peripheral nerve repair. *J Biomater Appl*. **2015**;*29*:1145.
15. Chen YJ, Cheng FC, Chen CJ, Su HL, Sheu ML, Sheehan J, Pan HC. Down-regulated expression of magnesium transporter genes following a high magnesium diet attenuates sciatic nerve crush injury. *Neurosurgery*. **2019**;*84*:965.
16. Hu T, Xu H, Wang C, Qin H, An Z. Magnesium enhances the chondrogenic differentiation of mesenchymal stem cells by

inhibiting activated macrophage-induced inflammation. *Sci Rep*. **2018**;*8*:3406.
17. Yao Z, Yuan W, Xu J, Tong W, Mi J, Ho PC, Chow DHK, Li Y, Yao H, Li X, Xu S, Guo J, Zhu Q, Bian L, Qin L. Magnesium-encapsulated injectable hydrogel and 3D-engineered polycaprolactone conduit facilitate peripheral nerve regeneration. *Adv Sci (Weinh)*. **2022**;*9*:e2202102.
18. Huang J, Zhang G, Li S, Li J, Wang W, Xue J, Wang Y, Fang M, Zhou N. Endothelial cell-derived exosomes boost and maintain repair-related phenotypes of Schwann cells via miR199-5p to promote nerve regeneration. *J Nanobiotechnol*. **2023**;*21*:10.
19. Chen B, Banton MC, Singh L, Parkinson DB, Dun XP. Single cell transcriptome data analysis defines the heterogeneity of peripheral nerve cells in homeostasis and regeneration. *Front Cell Neurosci*. **2021**;*15*:624826.
20. Cao S, Wei Y, Yao Z, Yue Y, Deng J, Xu H, Sheng W, Yu F, Liu P, Xiong A, Zeng H. A bibliometric and visualized analysis of nanoparticles in musculoskeletal diseases (from 2013 to 2023). *Comput Biol Med*. **2024**;*169*:107867.
21. Yao Z, Xu J, Shen J, Qin L, Yuan W. Biomimetic hierarchical nanocomposite hydrogels: from design to biomedical applications. *J Compos Sci*. **2022**;*6*:340.
22. Fei J, Wen X, Lin X, Saijilafu, Wang W, Ren O, Chen X, Tan L, Yang K, Yang H, Yang L. Biocompatibility and neurotoxicity of magnesium alloys potentially used for neural repairs. *Mater Sci Eng C Mater Biol Appl*. **2017**, *78*, 1155.
23. Deng R, Luo Z, Rao Z, Lin Z, Chen S, Zhou J, Zhu Q, Liu X, Bai Y, Quan D. Decellularized extracellular matrix containing electrospun fibers for nerve regeneration: a comparison between core-shell structured and preblended composites. *Adv Fiber Mater*. **2022**;*4*:503.
24. Xue J, Xie J, Liu W, Xia Y. Electrospun nanofibers: new concepts, materials, and applications. *Acc Chem Res*. **1976**;*2017*:50.
25. Fang Y, Wang C, Liu Z, Ko J, Chen L, Zhang T, Xiong Z, Zhang L, Sun W. 3D printed conductive multiscale nerve guidance conduit with hierarchical fibers for peripheral nerve regeneration. *Adv Sci (Weinh)*. **2023**;*10*:e2205744.
26. Ma T, Hao Y, Li S, Xia B, Gao X, Zheng Y, Mei L, Wei Y, Yang C, Lu L, Luo Z, Huang J. Sequential oxygen supply system promotes peripheral nerve regeneration by enhancing Schwann cells survival and angiogenesis. *Biomaterials*. **2022**;*289*:121755.
27. Dong X, Wu P, Yan L, Liu K, Wei W, Cheng Q, Liang X, Chen Y, Dai H. Oriented nanofibrous P(MMD-co-LA)/Deferoxamine nerve scaffold facilitates peripheral nerve regeneration by regulating macrophage phenotype and revascularization. *Biomaterials*. **2022**;*280*:121288.
28. Yuan Z, Wei P, Huang Y, Zhang W, Chen F, Zhang X, Mao J, Chen D, Cai Q, Yang X. Injectable PLGA microspheres with tunable magnesium ion release for promoting bone regeneration. *Acta Biomater*. **2019**;*85*:294.
29. Li X, Dai B, Guo J, Zhu Y, Xu J, Xu S, Yao Z, Chang L, Li Y, He X, Chow DHK, Zhang S, Yao H, Tong W, Ngai T, Qin L. Biosynthesized bandages carrying magnesium oxide nanoparticles induce cortical bone formation by modulating endogenous periosteal cells. *ACS Nano*. **2022**;*16*:18071.
30. Xiao W, Chen Y, Pan G, Yan J, Zhang J, Gao J. Hydrophobic, hemostatic and durable nanofiber composites with a screw-like surface architecture for multifunctional sensing electronics. *Adv Fiber Mater*. **2023**;*5*:2040.
31. Zou JL, Liu S, Sun JH, Yang WH, Xu YW, Rao ZL, Jiang B, Zhu QT, Liu XL, Wu JL, Chang C, Mao HQ, Ling EA, Quan DP, Zeng YS. Peripheral nerve-derived matrix hydrogel promotes remyelination and inhibits synapse formation. *Adv Funct Mater*. **2018**;*28*:1.
32. Xu S, Zhang Y, Dai B, Rao J, Deng F, Zhang Sa, Shao H, Li X, Jin Z, Liang T, Yang Y, Li Y, Chen Z, Tong W, Xu J, Ning C, Qin L. Green-prepared magnesium silicate sprays enhance the repair of burn-skin wound and appendages regeneration in rats and minipigs. *Adv Funct Mater*. **2023**, *34*, 2307439.
33. Xu J, Hu P, Zhang X, Chen J, Wang J, Zhang J, Chen Z, Yu MK, Chung YW, Wang Y, Zhang X, Zhang Y, Zheng N, Yao H, Yue J, Chan HC, Qin L, Ruan YC. Magnesium implantation or supplementation ameliorates bone disorder in CFTR-mutant mice through an ATF4-dependent Wnt/beta-catenin signaling. *Bioact Mater*. **2022**;*8*:95.
34. Fazal SV, Gomez-Sanchez JA, Wagstaff LJ, Musner N, Otto G, Janz M, Mirsky R, Jessen KR. Graded elevation of c-Jun in Schwann cells in vivo: gene dosage determines effects on development, remyelination, tumorigenesis, and hypomyelination. *J Neurosci*. **2017**;*37*:12297.
35. Li Y, Yang B, Wang Y, Huang Z, Wang J, Pu X, Wen J, Ao Q, Xiao K, Wu J, Yin G. Postoperatively noninvasive optogenetic stimulation via upconversion nanoparticles enhancing sciatic nerve repair. *Nano Lett*. **2024**;*24*:5403.
36. Mohamed T, Colciago A, Montagnani Marelli M, Moretti RM, Magnaghi V. Protein kinase C epsilon activation regulates proliferation, migration, and epithelial to mesenchymal-like transition in rat Schwann cells. *Front Cell Neurosci*. **2023**;*17*:1237479.
37. Chang L, Yao H, Yao Z, Ho KK, Ong MT, Dai B, Tong W, Xu J, Qin L. Comprehensive analysis of key genes, signaling pathways and mirnas in human knee osteoarthritis: based on bioinformatics. *Front Pharmacol*. **2021**;*12*:730587.
38. Mi J, Xu JK, Yao Z, Yao H, Li Y, He X, Dai BY, Zou L, Tong WX, Zhang XT, Hu PJ, Ruan YC, Tang N, Guo X, Zhao J, He JF, Qin L. Implantable electrical stimulation at dorsal root ganglions accelerates osteoporotic fracture healing via calcitonin gene-related peptide. *Adv Sci*. **2022**;*9*:e2103005.
39. Qiu S, Rao Z, He F, Wang T, Xu Y, Du Z, Yao Z, Lin T, Yan L, Quan D, Zhu Q, Liu X. Decellularized nerve matrix hydrogel and glial-derived neurotrophic factor modifications assisted nerve repair with decellularized nerve matrix scaffolds. *J Tissue Eng Regen Med*. **2020**;*14*:931.
40. He FL, Qiu S, Zou JL, Gu FB, Yao Z, Tu ZH, Wang YY, Liu XL, Zhou LH, Zhu QT. Covering the proximal nerve stump with chondroitin sulfate proteoglycans prevents traumatic painful neuroma formation by blocking axon regeneration after neurotomy in Sprague Dawley rats. *J Neurosurg*. **2021**;*134*:1599.
41. Lin T, Liu S, Chen S, Qiu S, Rao Z, Liu J, Zhu S, Yan L, Mao H, Zhu Q, Quan D, Liu X. Hydrogel derived from porcine decellularized nerve tissue as a promising biomaterial for repairing peripheral nerve defects. *Acta Biomater*. **2018**;*73*:326.
42. Fiorentini D, Cappadone C, Farruggia G, Prata C. Magnesium: biochemistry, nutrition, detection, and social impact of diseases linked to its deficiency. *Nutrients*. **2021**;*13*(4):1136.
43. W X, J Y, Y S, Q W. The effect of magnesium deficiency on neurological disorders: a narrative review article. *Iran. J. Public Health*. **2019**, *48*, 379.
44. Cherian KN, Keynan JN, Anker L, Faerman A, Brown RE, Shamma A, Keynan O, Coetzee JP, Batail JM, Phillips A, Bassano NJ, Sahlem GL, Inzunza J, Millar T, Dickinson J, Rolle CE, Keller J, Adamson M, Kratter IH, Williams NR. Magnesium-ibogaine therapy in veterans with traumatic brain injuries. *Nat Med*. **2024**;*30*:373.
45. Wang JL, Xu JK, Hopkins C, Chow DH, Qin L. Biodegradable magnesium-based implants in orthopedics-a general review and perspectives. *Adv Sci*. **2020**;*7*:1902443.
46. Lu X, Cai H, Li YR, Zheng X, Yun J, Li W, Geng X, Kwon JS, Jiang HB. A systematic review and network meta-analysis of biomedical mg alloy and surface coatings in orthopedic application. *Bioinorg Chem Appl*. **2022**;*2022*:4529520.

47. Shin CH, Lee HY, Gyan-Barimah C, Yu JH, Yu JS. Magnesium: properties and rich chemistry for new material synthesis and energy applications. *Chem Soc Rev*. **2023**;*52*:2145.
48. Wu Q, Xu S, Wang F, He B, Wang X, Sun Y, Ning C, Dai K. Double-edged effects caused by magnesium ions and alkaline environment regulate bioactivities of magnesium-incorporated silicocarnotite in vitro. *Regen Biomater*. **2021**, *8*, rbab016.
49. Salzer J, Feltri ML, Jacob C. Schwann cell development and myelination. *CSH Perspect Biol*. **2024**;*16*(9):a041360.
50. Scherer SS, Svaren J. Peripheral nervous system (PNS) myelin diseases. *CSH Perspect Biol*. **2024**;*16*(5):a041376.
51. Yan Y, Yao R, Zhao J, Chen K, Duan L, Wang T, Zhang S, Guan J, Zheng Z, Wang X, Liu Z, Li Y, Li G. Implantable nerve guidance conduits: material combinations, multi-functional strategies and advanced engineering innovations. *Bioact Mater*. **2022**;*11*:57.
52. Sowa Y, Kishida T, Tomita K, Yamamoto K, Numajiri T, Mazda O. Direct conversion of human fibroblasts into Schwann cells that facilitate regeneration of injured peripheral nerve in vivo. *Stem Cells Transl Med*. **2017**;*6*:1207.
53. Gomez-Sanchez JA, Pilch KS, van der Lans M, Fazal SV, Benito C, Wagstaff LJ, Mirsky R, Jessen KR. After nerve injury, lineage tracing shows that myelin and Remak Schwann cells elongate extensively and branch to form repair schwann cells, which shorten radically on remyelination. *J Neurosci*. **2017**;*37*:9086.
54. Rattner A, Wang Y, Nathans J. Signaling pathways in neurovascular development. *Annu Rev Neurosci*. **2022**;*45*:87.
55. Rim EY, Clevers H, Nusse R. The Wnt pathway: from signaling mechanisms to synthetic modulators. *Annu Rev Biochem*. **2022**;*91*:571.
56. Liu J, Xiao Q, Xiao J, Niu C, Li Y, Zhang X, Zhou Z, Shu G, Yin G. Wnt/beta-catenin signalling: function, biological mechanisms, and therapeutic opportunities. *Signal Transduct Target Ther*. **2022**;*7*:3.
57. Shah R, Amador C, Chun ST, Ghiam S, Saghizadeh M, Kramerov AA, Ljubimov AV. Non-canonical Wnt signaling in the eye. *Prog Retin Eye Res*. **2023**;*95*:101149.
58. Liu YJ, Chen XF, Zhou LP, Rao F, Zhang DY, Wang YH. A nerve conduit filled with Wnt5a-loaded fibrin hydrogels promotes peripheral nerve regeneration. *CNS Neurosci Ther*. **2022**;*28*:145.
59. van Vliet AC, Lee J, van der Poel M, Mason MRJ, Noordermeer JN, Fradkin LG, Tannemaat MR, Malessy MJA, Verhaagen J, De Winter F. Coordinated changes in the expression of Wnt pathway genes following human and rat peripheral nerve injury. *PLoS ONE*. **2021**;*16*:e0249748.
60. Takahashi K, Yoshida T, Wakamori M. Periodontal ligaments enhance neurite outgrowth in trigeminal ganglion neurons through Wnt5a production induced by mechanical stimulation. *Am J Physiol Cell Physiol*. **2022**;*323*:C1704.
61. Li L, Hutchins BI, Kalil K. Wnt5a induces simultaneous cortical axon outgrowth and repulsive turning through distinct signaling mechanisms. *Sci Signal*. **2010**, *3*, pt2.
62. Li L, Hutchins BI, Kalil K. Wnt5a induces simultaneous cortical axon outgrowth and repulsive axon guidance through distinct signaling mechanisms. *J Neurosci*. **2009**;*29*:5873.
63. Yi S, Xu L, Gu X. Scaffolds for peripheral nerve repair and reconstruction. *Exp Neurol*. **2019**;*319*:112761.

Authors and Affiliations

Zhi Yao[1] · Ziyu Chen[1] · Xuan He[4] · Yihao Wei[1] · Junyu Qian[1] · Qiang Zong[2] · Shuxian He[3] · Lili Song[6] · Lijia Ma[7] · Sien Lin[8] · Linlong Li[8,9] · Lixiang Xue[5] · Siu Ngor Fu[2] · Jin Zhang[3] · Ye Li[2,9] · Deli Wang[1]

✉ Jin Zhang
J_Zhang929@fzu.edu.cn

✉ Ye Li
yeli@link.cuhk.edu.hk

✉ Deli Wang
wangdelinavy@163.com

[1] Department of Bone and Joint Surgery, Peking University Shenzhen Hospital, Shenzhen Peking University-The Hong Kong University of Science and Technology Medical Center, Shenzhen 518000, China

[2] Department of Rehabilitation Sciences, The Hong Kong Polytechnic University, Hong Kong SAR 999077, China

[3] College of Chemical Engineering, Fuzhou University, Fuzhou 350000, China

[4] Orthopedic Department, Peking University Third Hospital, Beijing 100000, China

[5] Cancer Center of Peking University Third Hospital, Center of Basic Medical Research, Institute of Medical Innovation and Research, Peking University Third Hospital, Beijing 100000, China

[6] Department of Hand and Microsurgery, Peking University Shenzhen Hospital, Shenzhen 518000, China

[7] Department of Spine Surgery, Peking University Shenzhen Hospital, Shenzhen 518000, China

[8] Musculoskeletal Research Laboratory of Department of Orthopaedics and Traumatology, Li Ka Shing Institute of Health Sciences, The Chinese University of Hong Kong, Hong Kong SAR 999077, China

[9] Centre for Regenerative Medicine and Health, Hong Kong Institute of Science & Innovation, Chinese Academy of Sciences, Hong Kong SAR 999077, China